JOURNAL OF MATERIALS SCIENCE 10 (1975) 1049–1081

Review
Indentation fracture: principles and applications

BRIAN LAWN*, RODNEY WILSHAW
Division of Materials Science, School of Applied Sciences, University of Sussex, Falmer, Sussex, UK

The basic principles and practical applications of indentation fracture are reviewed.

1. Introduction

The microcracking which occurs in the contact loading of brittle solids is a feature basic to a wide range of applied phenomena. The shaping of brittle materials by cutting, abrasion, grinding and drilling; the damage and subsequent erosion and wear of surfaces; the creation of particulate matter by comminution, fragmentation, milling, etc.: all are intimately tied up with the manner in which small-scale fractures initiate and propagate within highly localized stress fields. Central to the scientific evaluation of such phenomena is the indentation test, now widely adopted as a standard indicator of material "hardness" [1, 2]. However, largely because of a long-standing preoccupation with empirical applications in quality control, our fundamental understanding of the indentation test in terms of actual deformation mechanisms has been strangely slow in developing. Nowhere is this more evident than in the case of indentation-induced fracture; the characteristic microcrack patterns tend to be viewed at best as something of a curiosity, more often as a disruptive element to be avoided at all cost.

Yet from an historical standpoint the problem of indentation fracture evolves from a background of well-founded principles. As early as 1881, Hertz, motivated by the question of the physical significance of hardness, analysed the elastic contact between two curved bodies, and subsequently described qualitatively the cone-shaped crack that runs around the contact circle and spreads downward into one of the bodies at critical loading [3]. The most widely used configuration of the Hertzian test today is that of a relatively hard sphere (indenter) loaded onto a flat block or slab (specimen). One great advantage of this type of system lies in the fact that the elastic stress field, although complex, is well defined up to the point of fracture. The system thereby lends itself to an analysis in terms of the fundamental Griffith theory of fracture for elastic-brittle solids [4]: in this view the crack is assumed to initiate at some "dominant flaw" in the specimen surface, and thence to propagate into the characteristic cone in accordance with the requirements of an energy-balance condition.

However, more common in current indentation testing is the "sharp" indenter, e.g. cone or pyramid, favoured because of the geometrical similarity of the residual impressions; the contact pressure is then independent of indent size, and thus affords a convenient measure of the hardness [5]. In this case the elastic stress field is singular about the indenter point, which leads inevitably to the operation of such irreversible deformation modes as plastic or viscous flow, structural densification, etc. These modes are activated by the large components of shear and hydrostatic compression in the singular field, and account for both the existence of the residual impression and the initiation of any ensuing microfractures. The modified stress field through which the cracks must ultimately propagate is relatively *ill*-defined, and tends to give rise to a more complex fracture pattern than in the Hertzian case.

One point that needs to be emphasized at the

---

* On study leave, from School of Physics, University of New South Wales, Kensington, New South Wales, Australia.

outset is that a component of tension, however small, is unavoidable in *all* indentation fields. This raises the issue of brittleness, for cracking will then certainly occur if suitable initiating sources are present. It is also necessary to identify some important test variables. For instance, to establish the nature of the indentation stress field one specifies details of the contact geometry, load rate, etc. Similarly, to take into account extraneous influences on the fracture properties one specifies the temperature and state of the environment. These and other factors are responsible for a complex diversity in general indentation fracture behaviour, a diversity which is not easily accommodated within a rational descriptive framework.

Nevertheless, recent developments in the quantitative evaluation of indentation processes have opened up the way to a broad view of the problem. Moreover, apart from providing the basis of a model system for discussing the applied phenomena mentioned earlier, these developments have shown the indentation test to be a potentially valuable tool in the measurement of intrinsic fracture parameters of brittle solids. In particular, basic information on fracture-surface energies and crack-velocity functions may be extracted from the experimental observations. It is in this context that the present review is conceived.

2. Indentation stress fields

The first requirement of any soundly-based theory of indentation fracture is a detailed knowledge of the stress field within the loaded system. This demands a close look at the nature of the contact zone. Here the shape of the indenter is a vital factor in determining the boundary conditions for the field, as indicated in Fig. 1 [6, 7]. Basically, we can expect very high gradients, if not singularities, in the stresses about any sharp points or edges of an ideally elastic contact, which may be relieved to a greater or lesser extent by localized inelastic deformation. The applied forces may contain both normal and tangential components, the latter of which can arise from either oblique loading or interfacial friction between indenter and specimen. Again, the applied forces may vary with time within the duration of the test, giving rise to extremes of static or dynamic loading conditions. Mechanical anisotropy is yet another factor to be considered, particularly in the indentation of single crystals. While we shall devote some attention to most of these points in the following discussions, for the purpose of emphasizing the more important principles our approach will be to concentrate on the simplest model configurations as much as possible.

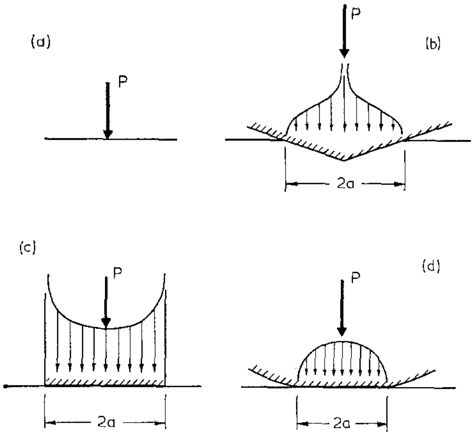

Figure 1 Elastic contact pressure distributions for various indentation systems: (a) point load, (b) sharp indenter, (c) flat punch, (d) sphere (or cylinder). P and a characterize extent of applied loading and resulting contact respectively.

Our foremost aim here must be to investigate the distribution of the stress component primarily responsible for the operation of fracture processes, namely the tensile stress. A survey of two classical elastic indentation fields, involving in the first case the idealized point indenter of Fig. 1a and in the second case the spherical indenter of Fig. 1d, will suffice to bring out the essential features. (Of course, in accordance with the principle of superposition for linear fields, it is possible to view all contact configurations in Fig. 1 in terms of an appropriate distribution of point loads at the specimen surface.) At the same time, it is also important that we should have some feeling for the distribution of shear and hydrostatic components, for these will determine the extent of irreversible deformation within the field. Comments on the complex and poorly understood role of such deformation in modifying the stress distributions will be brief and qualitative.

One begins the stress analysis by introducing convenient *scaling* parameters for the general field: the *spatial* contact scales with some characteristic dimension, a say (Fig. 1); then the *intensity* of the stresses scales with the mean contact pressure,

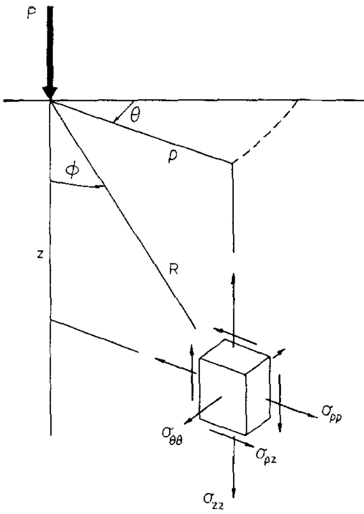

Figure 2 Co-ordinate system for indentation stress field.

$$p_0 = \frac{P}{\alpha\pi a^2}, \tag{1}$$

with P the applied load and α a dimensionless constant reflecting the indenter geometry; for axially symmetric indenters, $\alpha = 1$.

2.1. Point-force indenters – Boussinesq elastic field

Consider an isotropic, linear elastic half-space subjected to a normal point load P (Fig. 1a). The solutions for the stress field in this configuration were first given by Boussinesq in 1885 [8], and assume the simple, general form

$$\sigma_{ij} = \left(\frac{P}{\pi R^2}\right)[f_{ij}(\phi)]_\nu \tag{2}$$

when expressed in terms of the curvilinear coordinates of Fig. 2 [9]. That is, the magnitude of the stresses is proportional to the applied load and to the inverse square of the radial distance from the point of contact, times some independent angular function which is itself a function of Poisson's ratio ν. The singularity at $R = 0$ in Equation 2 is a characteristic of the Boussinesq field, and a consequence of the implicit assumption of a zero contact area ($a = 0$) for supporting the applied load. The situation is not unlike that which prevails at the tip of an ideally sharp crack [10]. In reality, non-linear, inelastic deformation will operate to relieve the high stress concentration about the singular point, and in so doing distribute the load over a non-zero contact area ($a > 0$). It becomes convenient to rewrite Equation 2 in alternative, normalized form,

$$\frac{\sigma_{ij}}{p_0} = \alpha\left(\frac{a}{R}\right)^2[f_{ij}(\phi)]_\nu \, . \tag{3}$$

Of particular interest is the case where the contact complies with the principle of geometrical similarity, for the field intensity is then governed explicitly by the indentation hardness $H \approx p_0 = \text{const}$. It is standard practice, again in analogy with the sharp-crack problem, to exclude hypothetically a small, non-linear contact zone $R \approx a$ from the Boussinesq field, and to view the deformation within in terms of a "blunting" of the indenter tip; the linear solutions then provide increasingly accurate representations of the real situation as one proceeds outward from this zone (St. Venant's principle).

The essential features of the field are illustrated in Figs. 3 and 4, for the case $\nu = 0.25$ (a typical value for brittle solids). We investigate the *directions* of the principal stresses, σ_{11}, σ_{22} and σ_{33}, by means of the stress-trajectory plots in Fig. 3. The three families of trajectories are labelled such that $\sigma_{11} \geqslant \sigma_{22} \geqslant \sigma_{33}$ nearly everywhere. Similarly, we investigate the *distribution* of the principal stresses by means of the contour plots in Fig. 4. The components σ_{11} and σ_{33}, acting within symmetry planes through the load axis, are wholly tensile and compressive respectively. The component σ_{22}, a "hoop stress", is tensile in a region below the indenter but compressive near the surface. We note

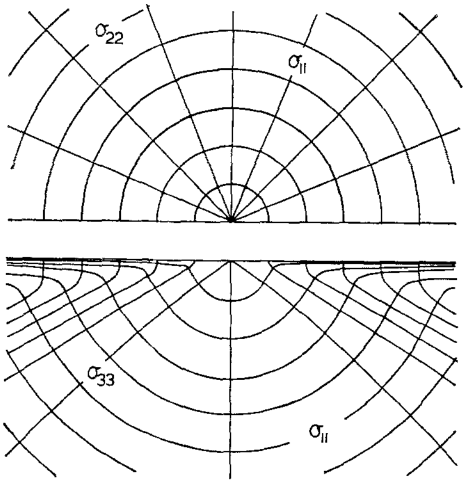

Figure 3 Half-surface view (top) and side view (bottom) of stress trajectories in Boussinesq field. Plotted for $\nu = 0.25$. (After [9].)

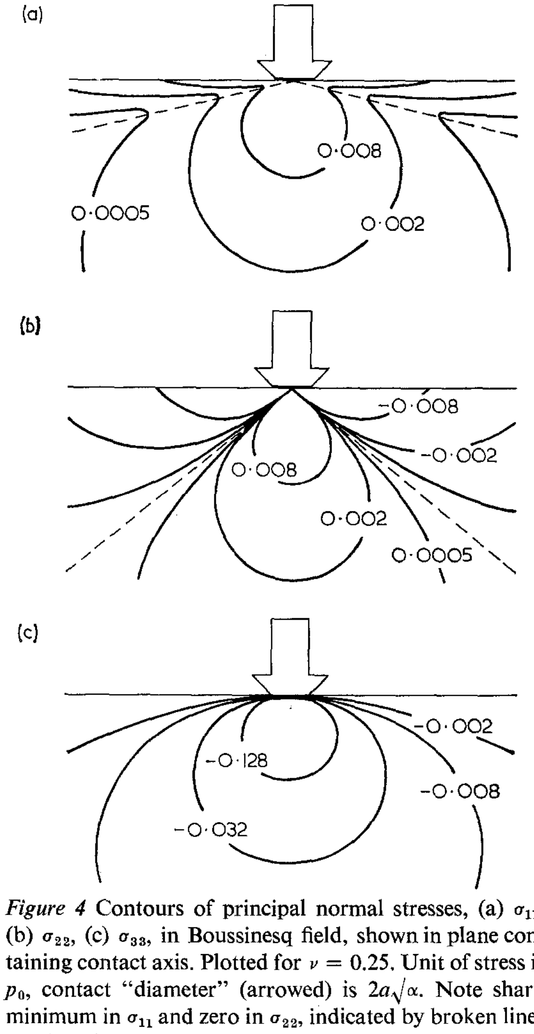

Figure 4 Contours of principal normal stresses, (a) σ_{11}, (b) σ_{22}, (c) σ_{33}, in Boussinesq field, shown in plane containing contact axis. Plotted for $\nu = 0.25$. Unit of stress is p_0, contact "diameter" (arrowed) is $2a\sqrt{\alpha}$. Note sharp minimum in σ_{11} and zero in σ_{22}, indicated by broken lines in (a) and (b) respectively. (After [9].)

maxima in the tensile stresses at $\phi = \pi/2$ (σ_{11}) and $\phi = 0$ ($\sigma_{11} = \sigma_{22}$).

From the three principal normal stresses, an evaluation of the principal shear and hydrostatic compressive stresses is straightforward; along the contact axis, where maxima once more occur, these components typically exceed those of the tensile stresses by several times [9].

2.2. Spherical indenters – Hertzian elastic field and its variants

The case of a spherical indenter loaded onto a flat specimen, by virtue of its ease in application and avoidance of complicating singularities, is by far the most extensively studied of elastic contact configurations. We outline first the features of the ideal Hertzian field, and then discuss some of the modifications that occur in important practical situations.

2.2.1. The ideal Hertzian field

Consider now an isotropic, linear elastic half-space subjected to normal loading by a smooth spherical indenter of radius r. The original Hertz analysis gave explicit quantitative consideration to only the surface stress conditions [3]. Taking E and E' as the Young's modulus of specimen and sphere respectively, and likewise ν and ν' the Poisson's ratio, the radius a of the circular elastic contact is given by

$$a^3 = \frac{4kPr}{3E}, \tag{4}$$

where P is the applied normal load and k is a dimensionless constant,

$$k = \frac{9}{16}\left[(1-\nu^2) + (1-\nu'^2)\frac{E}{E'}\right]. \tag{5}$$

The distance of mutual approach Z between contacting bodies is given by

$$Z^3 = \left(\frac{4k}{3E}\right)^2 \frac{P^2}{r}. \tag{6}$$

These three equations are sufficient to specify the loading conditions for any commonly used ball indentation arrangement [11].

Within the contact circle the applied load is distributed as a hemisphere of compressive stress (Fig. 1d). The maximum tensile stress in the specimen surface occurs at the edge of the

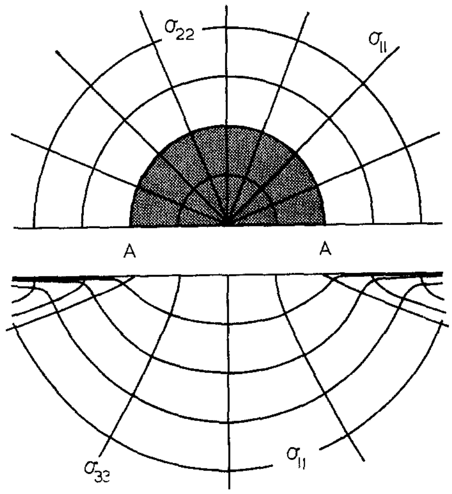

Figure 5 Half-surface view (top) and side view (bottom) of stress trajectories in Hertzian field. Plotted for $\nu = 0.33$. AA denotes diameter of contact. Cf. Fig. 3. (After [14].)

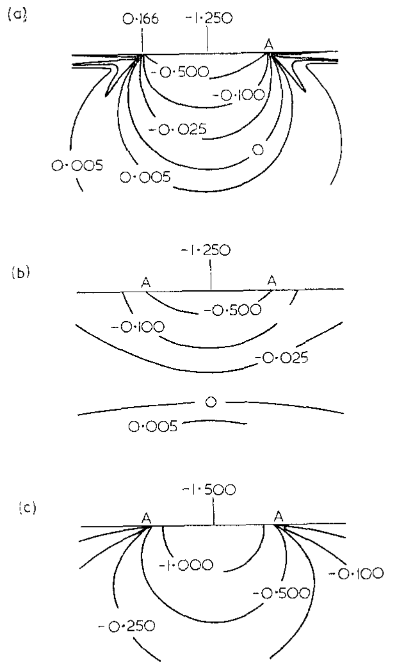

Figure 6 Contours of principal normal stresses, (a) σ_{11}, (b) σ_{22}, (c) σ_{33}, in Hertzian field, shown in plane containing contact axis. Plotted for $\nu = 0.33$. Unit of stress is p_0, contact diameter AA is $2a$. Cf Fig. 4. (After [14].)

contact and is radially directed; it falls off with radial distance ρ (Fig. 2) outside the contact circle according to

$$\frac{\sigma_{\rho\rho}}{p_0} = \left(\frac{1-2\nu}{2}\right)\left(\frac{a}{\rho}\right)^2, \quad (\rho \geqslant a) \cdot \qquad (7)$$

In 1904 Huber [12] extended the Hertz analysis, and produced complete stress field solutions in the form

$$\frac{\sigma_{ij}}{p_0} = \left[g_{ij}\left(\frac{\rho}{a}, \frac{z}{a}\right)\right]_{\nu} \cdot \qquad (8)$$

Proceeding as with the Boussinesq case, we plot in Figs. 5 and 6 trajectories and contours for the functions of Equation 8 corresponding to the three principal stresses [13, 14], this time for $\nu = 0.33$. Comparing these plots with their counterparts in Figs. 3 and 4, it is apparent that the precise form of the applied load distribution can have a profound influence on the nature of the near-contact field. With regard to the directions of the principal stresses, the main change appears to be a minor "flattening" of the σ_{11} trajectories immediately below the contact area. More dramatic changes are seen in the magnitudes of the stresses, in which the tensile components tend to be locally suppressed. Both σ_{11} and σ_{22} become compressive to a depth $\approx 2a$, below which a rapid convergence to Boussinesq values occurs; Fig. 7 illustrates this convergence for the stress $\sigma_{\theta\theta} = \sigma_{11} = \sigma_{22}$ along the contact axis. In the surface region outside the contact no sign reversal in the stresses is evident, but extremely high stress gradients are set up at the edge of contact; these gradients become especially severe for small contact areas.

2.2.2. *Time-dependent loading*

Because the fracture of brittle solids can be highly rate dependent (Section 3) it is important to pay some attention to the time characteristics of the applied loading. A convenient way of doing this is to follow the variation of the contact velocity, $\dot a = \mathrm{d}a/\mathrm{d}t$. We do this for four common modes of indenter loading below [11]:

(i) *Constant load rate* ($\dot P = \mathrm{d}P/\mathrm{d}t = $ const.). A linear speed, dead-weight loading machine operates in this mode [15]. Differentiating Equation 4 with respect to time, we obtain

$$\dot a(\dot P, t) = \left(\frac{4kr\dot P}{9Et^2}\right)^{1/3} \cdot \qquad (9)$$

(ii) *Constant displacement rate* ($\dot Z = \mathrm{d}Z/\mathrm{d}t = $ const.). This is the mode corresponding to those machines (e.g. Instron) which operate at constant cross-head speed. For an effectively rigid machine this speed is equivalent to $\dot Z$, in which case Equations 4 and 6 yield

$$\dot a(\dot Z, t) = (r\dot Z/4t)^{1/2} \, . \qquad (10)$$

(iii) *Static load* ($P = $ const.). "Instantaneous" loading to a prescribed level, thereafter held fixed, is useful in "static fatigue" testing; these conditions are given formally by

$$\left.\begin{aligned} \dot a &\rightarrow \infty, \quad (\delta t \leqslant t \leqslant 0) \\ \dot a &= 0, \quad (0 \leqslant t \leqslant t_\mathrm{D}) \end{aligned}\right\} \qquad (11)$$

with $t_\mathrm{D} (\gg \delta t)$ the duration of loading.

(iv) *Free-fall impact.* Release of the sphere from a height h involves a relatively complicated time-dependent function [11], which we write simply as

$$\dot a = \dot a(h, t) \, . \qquad (12)$$

The function $\dot a(t)$ is plotted in Fig. 8 for all but the third mode above, using typical values for the test variables. Broadly, if the contact circle expands at a rate not approaching the velocity of elastic waves (i.e. if $\dot a \ll 10^3$ to 10^4 m sec^{-1}, typically), the stress field may be considered

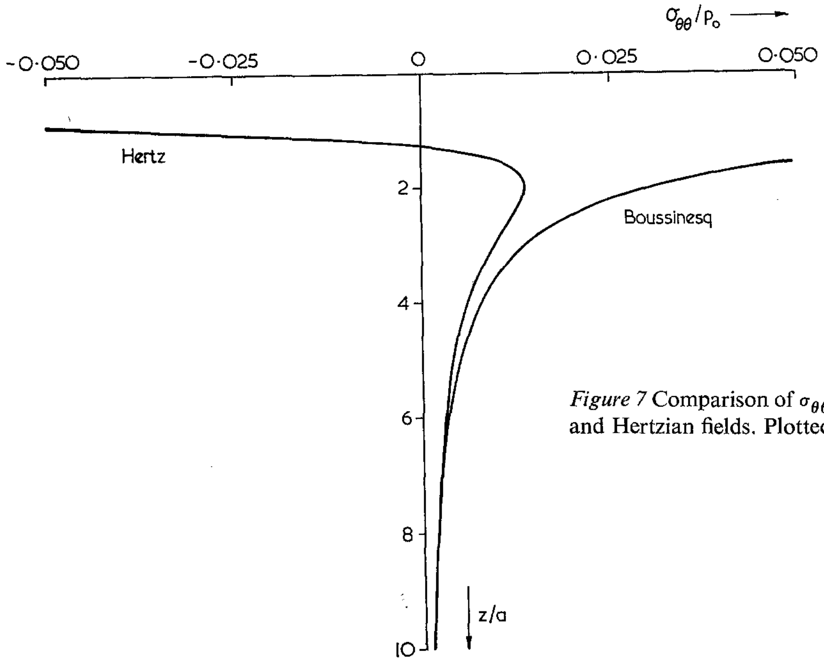

Figure 7 Comparison of $\sigma_{\theta\theta}(z)$ stress terms for Boussinesq and Hertzian fields. Plotted for $\nu = 0.25$. (After [9].)

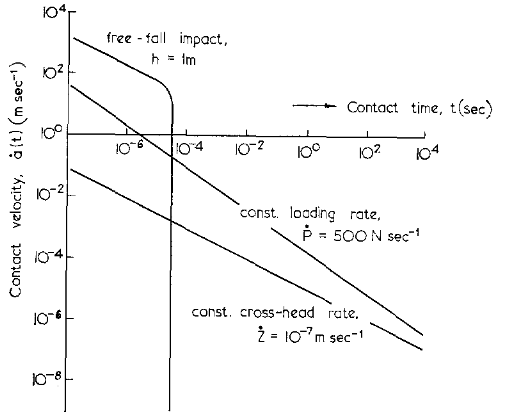

Figure 8 Plots of Hertzian contact velocity $\dot{a}(t)$ for three specific loading modes. Calculations for tungsten carbide sphere, $r = 6.35$ mm, on glass, $E = 7.0 \times 10^{10}$ N m^{-2}, $k = 0.55$.

quasistatic, and the solutions of Figs. 5 and 6 taken from equilibrium equations of elasticity will provide an adequate description of the system. In certain projectile impacting systems a fully dynamic situation prevails [16], the solution of which is generally intractable.

2.2.3. Tangential friction forces – elastic mismatch at static interface

In most indentation tests it is usual to choose materials such that the elastic stiffness of the indenter exceeds that of the specimen ($E' > E$), in order to safeguard against permanent deformation of the indenter. Upon normal loading, the opposing contact surfaces will both displace radially inward, owing to the action of the compressive radial stress σ_{22} within $\rho < a$ (Figs. 5 and 6). The more compliant specimen will want to undergo greater displacement than the indenter, but will be restrained from doing so by frictional tractions at the interface. This will give rise to a distribution of outwardly acting tangential forces at the contact surface of the specimen, to be superposed onto the hemispherical distribution of normal Hertzian forces (an equal and opposite set of forces will act on the corresponding indenter surface).

The modifying effect of the tangential tractions on the stress field has been discussed by Johnson *et al.* [17]. Their analysis gives explicit attention to only the radial stresses in the specimen surface outside the contact area, and to only two limiting situations: (a) "no slip", where the friction is sufficiently high that slip is prevented everywhere at the interface, in which case the modified stress distribution is determined entirely by an elastic mismatch parameter,

$$\kappa = \frac{(1 - 2\nu)/\mu - (1 - 2\nu')/\mu'}{(1 - \nu)/\mu + (1 - \nu')/\mu'}, \qquad (13)$$

with μ, μ' the shear modulus of specimen and

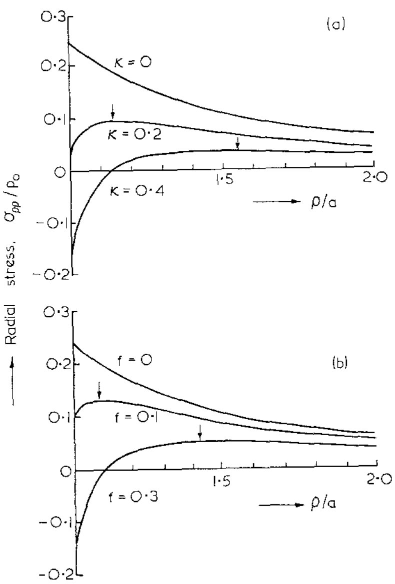

Figure 9 Effect of elastic mismatch between indenter and specimen on surface radial stress in Hertzian field; (a) no slip, (b) complete slip. Arrows indicate maximum tension. Plotted for $\nu = 0.25$. (After [17].)

indenter respectively; (b) "complete slip", where the friction is sufficiently low that slip occurs everywhere, so that the coefficient of static friction, f, becomes the determining parameter. Fig. 9 illustrates the two situations in their effect on the radial tension; we note the tendency for the maximum stress to diminish and to move outward from the contact circle as the parameters κ and f increase from zero. More generally, slip will occur over only part of the contact area (i.e. over an annulus); the intermediate situation, determined by the ratio f/κ, is a complex problem which has not yet been solved. In the special case of elastic symmetry, i.e. indenter and specimen of like material, we have $\kappa = 0$, the one configuration in which the ideal Hertzian field analysis remains strictly valid.

A further mismatch effect at the contact interface is treated in the paper by Johnson *et al.* This is the situation where the contacting surfaces are topographically rough, on a scale small compared to that of the contact itself. Making use of an earlier elasticity analysis for such surfaces [18], they are able to show that the effect of roughness is similar to that of interfacial friction, but generally of relatively insignificant magnitude.

2.2.4. Tangential friction forces – sliding interface

Suppose now that the spherical indenter is made to translate across the specimen surface at some steady speed. Once more frictional tractions will act to restrain mutual tangential displacements at the contact. This time the resultant distribution of tangential forces will act on the specimen in the direction of motion of the indenter.

The effect of sliding tractions on the stress field has been treated in depth by Hamilton and Goodman [19], for the case of complete slip. In this configuration the contact geometry remains unaffected by the friction, but the maximum radial tension at the trailing edge of the indenter is enhanced markedly according to

$$\frac{\sigma_{\rho\rho}}{p_0} = \left(\frac{1-2\nu}{2}\right)(1 + Af), \qquad (14)$$

where f is now strictly the coefficient of kinetic friction, and

$$A = \frac{3\pi(4+\nu)}{8(1-2\nu)}. \qquad (15)$$

Hamilton and Goodman also provide exact

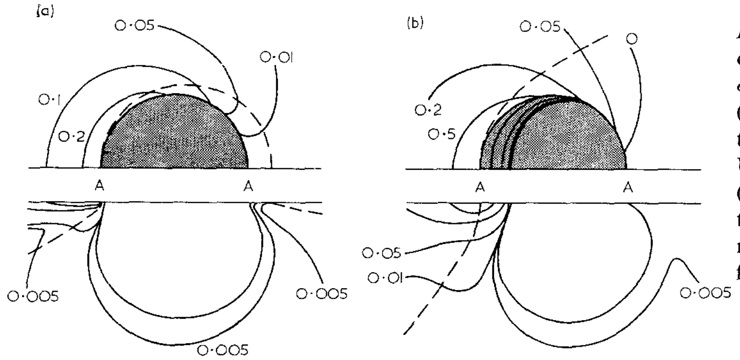

Figure 10 Half-surface view and side view of contours of greatest principal stress, σ_{11}, in elastic specimen in contact (diameter AA) with sliding sphere (motion left to right); (a) $f = 0.1$, (b) $f = 0.5$. Unit of stress is p_0. Dashed lines are σ_{22} (surface view) and σ_{33} (side view) stress trajectories drawn from place of maximum tensile stress in specimen. Plotted for $\nu = 0.33$. (After [20].)

solutions for the complete stress-field. Plots of the greatest principal stress, σ_{11}, for $f = 0.1$ and 0.5 and $\nu = 0.33$, are accordingly shown in Fig. 10 [20]. Also plotted are trajectories of the lesser principal stresses, starting from the point of maximum tension in the field. We note the dramatic tendency to an enhanced tension in the wake of the indenter, and a corresponding suppression ahead, at the higher sliding friction. We note also corresponding tendencies to an increased spacing of stress contours, i.e. a reduction in stress *gradient*, below the trailing edge, and a deviation from axial symmetry of the stress trajectory patterns.

2.3. Inelastic deformation fields

As indicated in our earlier discussion of the Boussinesq field in Section 2.1, limited inelastic deformation will tend to occur about any high stress concentrations, especially singular points, in an otherwise elastic indentation field. Such a situation poses complex problems in the stress analysis, particularly as the indenter material increases in brittleness. In a great number of brittle systems the very nature of the inelastic deformation remains a highly contentious issue [2]; it is no simple matter to establish which of two basic, competing processes, shear-induced flow (either plastic or viscous) or pressure-induced densification (phase change, or compaction of an "open" microstructure), dominates within the small contact zone in any given material. Then, each deformation mode is characterized by its own, complicated, stress-strain response, typified by some limiting stress level (yield stress, densification pressure) attainable within the material. Moreover, the non-linear zone itself is encased within confining linear material, and is therefore subjected to an elastic constraint. The general non-linear indentation problem would appear to be insoluble.

Nevertheless, through the introduction of certain simplistic models, some progress has been made in the case of elastic-plastic materials. These models have recently been surveyed by Tabor [1] and Johnson [7]. The basic concepts are expressed in the scheme of Fig. 11, as proposed by Marsh [21]. The major simplifying assumption is that of spherical symmetry in the deformation field: immediately below the indenter one takes the material to behave as an outwardly expanding "core", exerting a uniform hydrostatic pressure on its surrounds; encasing the core is an ideally "plastic region", within which flow occurs according to some simple yield criterion; beyond the plastic region lies the elastic "matrix". With Y the yield stress of the indented material, the analysis gives

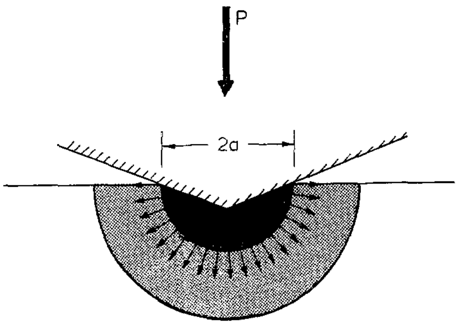

Figure 11 Model for elastic-plastic indentation problem. Dark region denotes "hydrostatic core", shaded region denotes "plastic zone", and surrounding region denotes "elastic matrix".

$$\frac{p_0}{Y} = h\left(\frac{E}{Y}\right), \tag{16}$$

where $h(E/Y)$ is a slowly-varying function of E/Y. However, the assumptions embodied in this model need to be examined critically. For example, with cone or pyramid indenters of small included angle the plastic material will tend to "pile-up" around the sides of the indenter, thereby destroying the spherical symmetry of the elastic-plastic boundary conditions; it has already become abundantly clear from the Hertzian study (Section 2.2) that small changes in the distribution of stresses at the elastic boundary can give rise to large changes in the near-field about the contact. This sensitivity to details in the model emphasizes the futility of any attempt at an exact stress analysis. Similar difficulties would be expected to arise in the case of deformation by densification, although analogous models have yet to be proposed for this mode.

One further complication that accompanies inelastic deformation deserves mention here. Because the inelastic material within the contact zone must (by definition) suffer permanent deformation after one complete loading and unloading cycle, the initial stress-free state in the surrounding elastic matrix can never be fully recovered. That is, a residual stress field will remain in the unloaded solid, and although its nature may be quite different from that corresponding to the fully loaded state, it will generally retain a significant tensile component.

3. Mechanics of indentation fracture

Given the stress field beneath an indenter, it is possible, in principle, to determine the mechanics of any ensuing fracture configuration. Following Griffith's pioneering paper on the rupture of brittle solids [4], two important aspects of the problem are identified: (i) *initiation* – how and where do the cracks start?; (ii) *propagation* – once started, what path do the cracks take, and what determines the extent of their growth? A detailed treatment of these fundamental issues in the context of modern-day brittle fracture theory is given elsewhere by the present authors [10], and only the more essential facts need be discussed here.

Of the two aspects, that of initiation is less amenable to quantification in terms of basic material properties. Initiation begins from "flaws", either pre-existing or induced by the indentation process itself. Pre-existing flaws occur typically as micron-scale microcracks; their nature and distribution depend in a complex way on the mechanical, thermal and chemical history of the material, but relate most commonly to the susceptibility of brittle surfaces to contact and handling damage. In many cases it is possible to exercise some control over the flaw population by means of an appropriate surface treatment, such as etching, to *remove* flaws, or abrasion, to *introduce* them. Deformation-induced flaws tend to nucleate at points of intense stress concentration ahead of locally impeded bands or zones of inelastically deformed material ("pile-up" concept). The general indentation specimen will be characterized by a diverse population of flaws just prior to fracture; whether or not a given flaw becomes critical will depend on its size, position and orientation within the tensile field.

Upon attaining some critical configuration, a "dominant" flaw develops into a well-defined propagating crack. This stage in the growth provides us with the greater amount of information on both fundamental and applied fracture processes, and will consequently receive the bulk of our attention in the fracture-mechanics analyses below. Fortunately, it is generally possible to specify adequate initial conditions for the propagation without a detailed knowledge of the nature of the starting flaw; one simply needs to nominate a starting location and "effective length" of an "equivalent microcrack". The conditions which determine the extension of a well-developed crack may then be expressed, for a quasistatic system, in terms of the total energy,

$$U = (-W_L + U_E) + U_S, \tag{17}$$

where W_L is the work of the applied forces, U_E is the elastic strain energy in the cracked body and U_S is the total surface energy of the crack walls. An energy interchange occurs between the mechanical term, $(-W_L + U_E)$, which decreases with extension, and the surface term, which correspondingly increases. In the "fracture-mechanics" formulation we consider the variation in these energy terms with respect to crack area C,

$$\frac{dU}{dC} = \frac{d(-W_L + U_E)}{dC} + \frac{dU_S}{dC} = -G + 2\Gamma, \tag{18}$$

where G is the mechanical-energy-release rate and Γ is the fracture-surface energy. In the case of an ideally brittle solid, where the work of creating the new crack surfaces contains no dissipative component, Γ reduces to the reversible surface energy γ.

3.1. Crack paths

An essential first step in any fracture-mechanics analysis is a knowledge of the prospective crack geometry. Let us consider an ideally brittle solid. Then, given a crack of characteristic area C, we assert that the relative orientation of an incremental extension δC be that which maximizes the quantity $G - 2\gamma$ in Equation 18 [10, 13]. For *isotropic* solids, this corresponds to a maximization of the mechanical-energy-release rate G. Thus, starting from a critical flaw, it becomes possible to trace out the ultimate path of the crack. Basically, the crack tends at any point to propagate along trajectories of lesser principal stresses in the *prior* field, thereby maintaining near-orthogonality to a major component of tension [13]. For *anisotropic* solids, notably single crystals, it is necessary to take into account the orientation dependence of both elastic constants (in so far as it affects G) and surface energy in determining maxima in $G - 2\gamma$. Clearly, in crystals with strong cleavage tendencies the anisotropy in γ will govern. Most generally, however, we expect some compromise between the tendencies for cracks to follow stress trajectories and cleavage planes.

3.1.1. Sharp indenters

There has been little genuine attempt by the hardness testing fraternity at a systematic description of the crack patterns surrounding impressions made by sharp indenters. The main reason for this appears to be the great diversity of patterns that arises as a result of minor variations in the test system (e.g. indenter shape, nature of environment, load rate, etc.). Yet certain underlying features of the fracture behaviour are quite general, and accordingly provide the basis for a working model [9].

In considering first the probable location of the starting flaw for an ensuing crack we make use of our knowledge of the indentation field, as outlined in Sections 2.1 and 2.3. We recall in particular the maxima in tensile stresses at the specimen surface and contact axis for the Boussinesq field (Fig. 4). Therefore, it seems reasonable to suppose that cracks will tend to inititiate at one of these favoured locations. In addition, however, we recall the tendency for inelastic deformation about singular points to both relieve and modify the local stresses, and, further, to nucleate its own flaws beneath the indenter. Thus, provided the surface does not contain severe handling damage, cracking would be expected to occur preferentially close to the contact axis. Finally, the possible influence of residual stresses on crack formation in the unloading specimen needs to be considered.

These conceptions accord with the basic sequence of subsequent crack propagation events, which we depict schematically in Fig. 12: (a) the sharp point of the indenter produces an inelastic deformation zone; (b) at some threshold, a deformation-induced flaw suddenly develops into a small crack, termed the *median vent*, on a plane of symmetry containing the contact axis; (c) an increase in load causes further, stable growth of the median vent; (d) on unloading, the median vent begins to close (but not heal); (e) in the course of indenter removal, sideways-extending cracks, termed *lateral vents*, begin to develop; (f) upon complete removal, the lateral vents continue their extension, toward the specimen surface, and may accordingly lead to chipping. Immediate reloading of the indenter closes the lateral vents, and reopens the median vents.

Micrographs of well-behaved vent systems are presented in Figs. 13 and 14 [9]. In both cases the cracks are confined to sub-surface regions of the specimen, i.e. they are not evident from an examination of the indenter surface. Fig. 13, a section view through an indentation in quartz, serves to confirm the classic features of the vent profile. Fig. 14 shows a side view of a median vent crack, in a polished glass block with the load still applied: the crack has grown straight downward along the axial σ_{33} stress trajectory (Fig. 3), orthogonally to the tensile stress $\sigma_{11} = \sigma_{22} = \sigma_{\theta\theta}$ at $\phi = 0$ (Fig. 2); at the same time, the crack has also grown sideways in a plane θ = const. along the σ_{11} trajectories, orthogonally everywhere to the hoop stress σ_{22} (Fig. 4b), but has clearly been restricted in this sideways expansion by the compressive lobes in the σ_{22} field close to the surface.

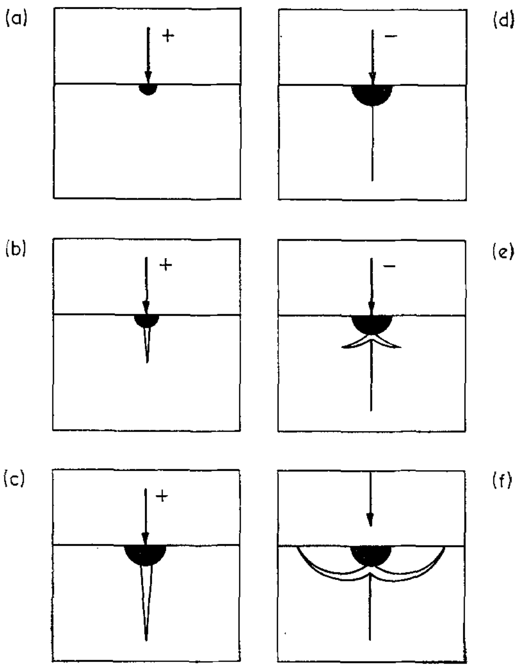

Figure 12 Schematic of vent crack formation under point indentation. Median vent forms during loading (+) half-cycle, lateral vents during unloading (−) half-cycle. Fracture initiates from inelastic deformation zone (dark region). (After [9].)

However, there are a number of variants in the detailed crack pattern which might be mentioned here. Fig. 15 depicts two common modifications of the median vent geometry. In the first, case (a), we sketch the behaviour observed at advanced stages in the normal loading, namely a sudden "breakthrough" of the crack to the specimen surface. This produces a characteristic radial trace on the surface, the length of which is comparable to the depth of the vent. An example

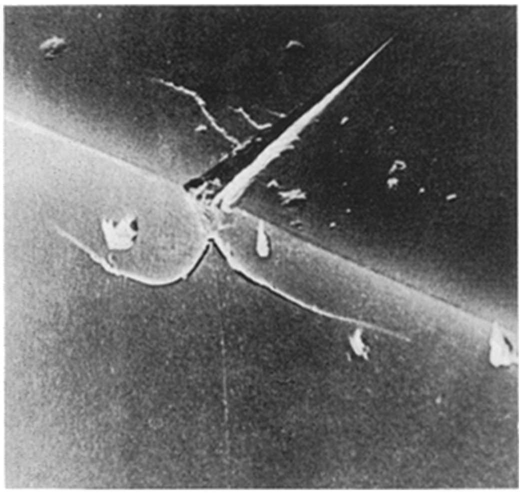

Figure 13 Scanning electron micrograph of Knoop impression in quartz (0001) surface. Section shows inelastic deformation zone immediately below surface impression, and associated vent pattern. Indenter load 2 N. Width of field 100 μm. (After [9].)

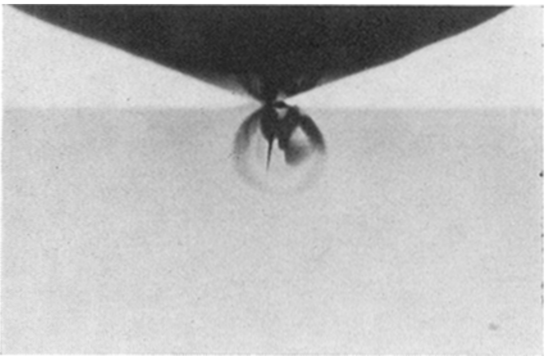

Figure 14 In situ photograph of Vickers indentation in soda-lime glass, taken in transmitted light. Indenter load 250 N. Width of field 11 mm. (After [9].)

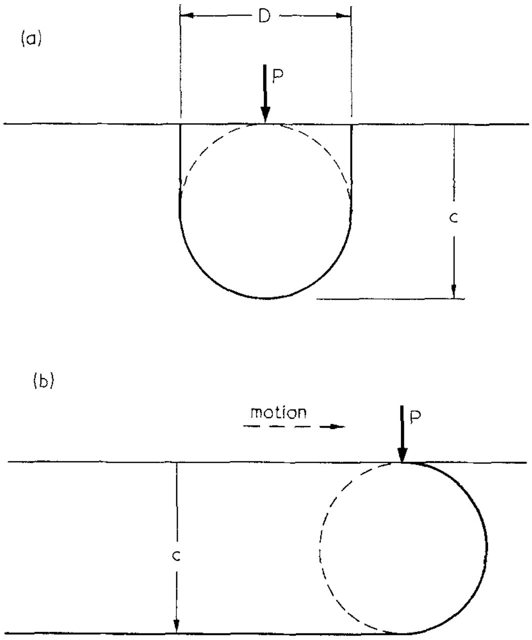

Figure 15 Schematic showing variants of median vent crack; (a) "breakthrough" to specimen surface at higher loading, producing radial surface trace $D \approx c$, and (b) "frictionless' translation across specimen surface, producing linear "score" depth c.

of such cracking is shown in Fig. 16, obtained by indenting a glass surface with a sharp cone. It is clear from this figure that several median vents can grow simultaneously: in isotropic systems, as illustrated here, the number of such vents will be limited only by the mutual stress-relieving influence of neighbours (hence producing a characteristic, near-equi-angled "star" pattern); in anisotropic systems, symmetry elements will impose themselves on the pattern, for the vents will prefer to form on planes of "easy cleavage" or planes containing sharp indenter edges. The surface pattern of radial cracking has hitherto been taken as an empirical indicator of material "brittleness" [22]. Turning now to case (b) in Fig. 15, we depict the effect of translating an effectively frictionless "point" indenter, e.g. a sharp-edged wheel, across the specimen surface; the nature of the indentation field remains essentially unchanged throughout the motion, as a result of which a single well-defined median vent traces out a linear "score" of uniform depth.

In all these variant cases the lateral vents complicate the picture. In Fig. 16, for instance, intersections with surface-linked median vents have led to a small degree of chipping. Since the lateral vents form on unloading [9, 23], they must be connected in some way with the residual stresses induced by the inelastic deformation zone. Our present understanding of the residual field is meagre, mainly for lack of knowledge of events within the zone itself. Further complications may also arise from other, spurious sources of microcracking, yet to be systematically documented [9].

3.1.2. Spherical indenters

By virtue of their ability to maintain a perfectly elastic contact up to the point of fracture, spherical indenters have been used widely in the scientific study of microfracture in brittle

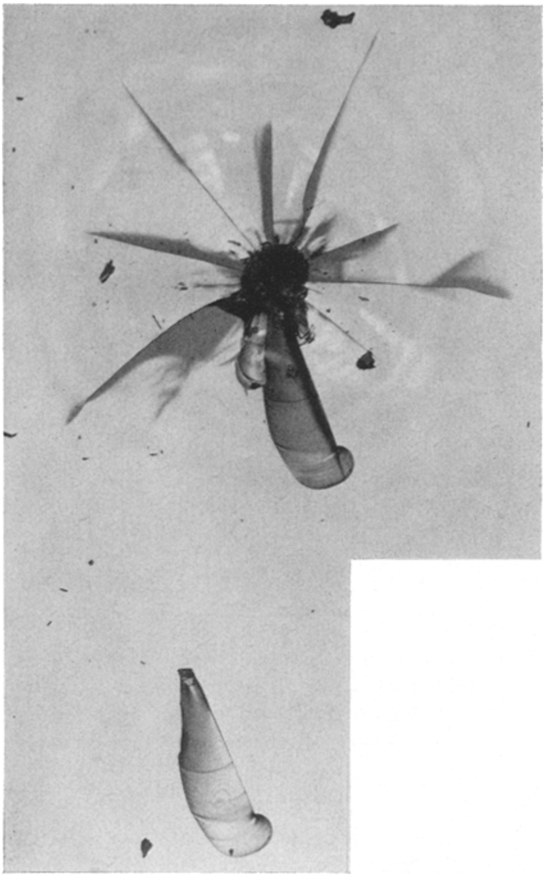

Figure 16 "Star" crack system in soda-lime glass, produced by conical indenter (included angle 120°). Note chipping where median and lateral vent cracks intersect. Note also dislodged fragment. Reflected light. Indenter load 160 N. Width of field 2 mm. (Courtesy of K. Phillips and I. B. Freeman.)

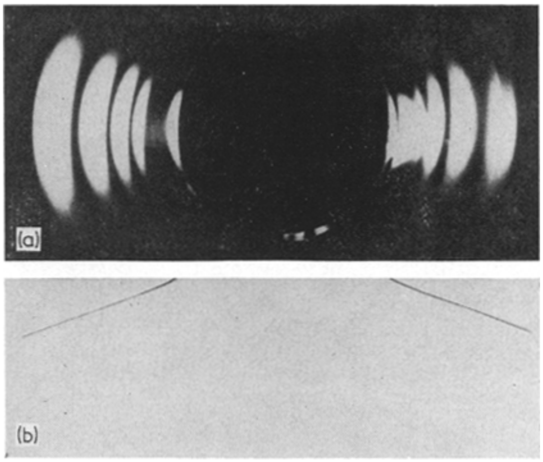

Figure 17 Cone crack in soda-lime glass, viewed (a) from below indented specimen at full load, in reflected light (critically directed to enter microscope objective), and (b) in profile, after section-and-etch of unloaded specimen. Diameter of surface crack 0.64 mm. (After [29].)

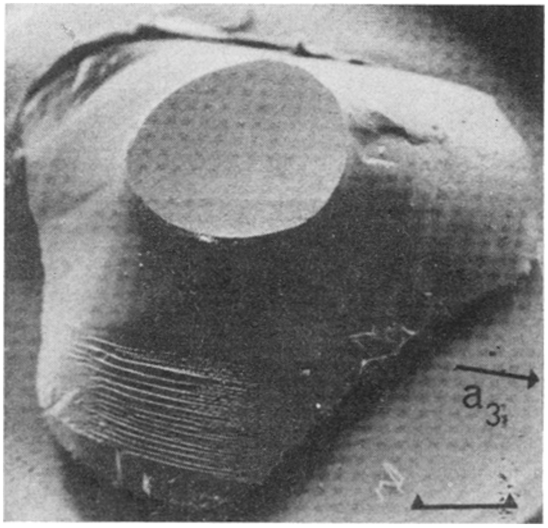

Figure 18 Scanning electron micrograph of Hertzian fracture removed from (0001) quartz slab by milling away back surface. $\mathbf{a}_3$ denotes ⟨0010⟩ direction. Marker 0.5 μm. (After [31].)

solids. The Hertzian elastic field, Section 2.2, provides an adequate basis for describing the entire crack geometry, free in most (but not all) cases of the complications which attend the onset of irreversible deformation.

Let us, therefore, begin with the ideal Hertzian configuration. In the absence of deformation-induced nucleation centres the fracture will initiate at a pre-existing flaw, almost certainly at the surface just outside the contact circle where the principal tensile component σ_{11} reaches its maximum (Fig. 6). The fracture begins its growth by running around the contact in an effectively uniform (symmetrical) σ_{11} field, closely following the circular σ_{22} stress trajectories (Fig. 5), and completes itself on the opposite side in the form of an "embryonic" surface ring crack [13, 14, 24]. Downward propagation of the surface ring occurs less readily because of the rapidly diminishing σ_{11} field beneath the free surface, but nevertheless proceeds subsequently along the σ_{33} trajectories to form the fully-developed Hertzian (truncated) cone.

The most systematic experimental studies of Hertzian fracture geometry have been carried out

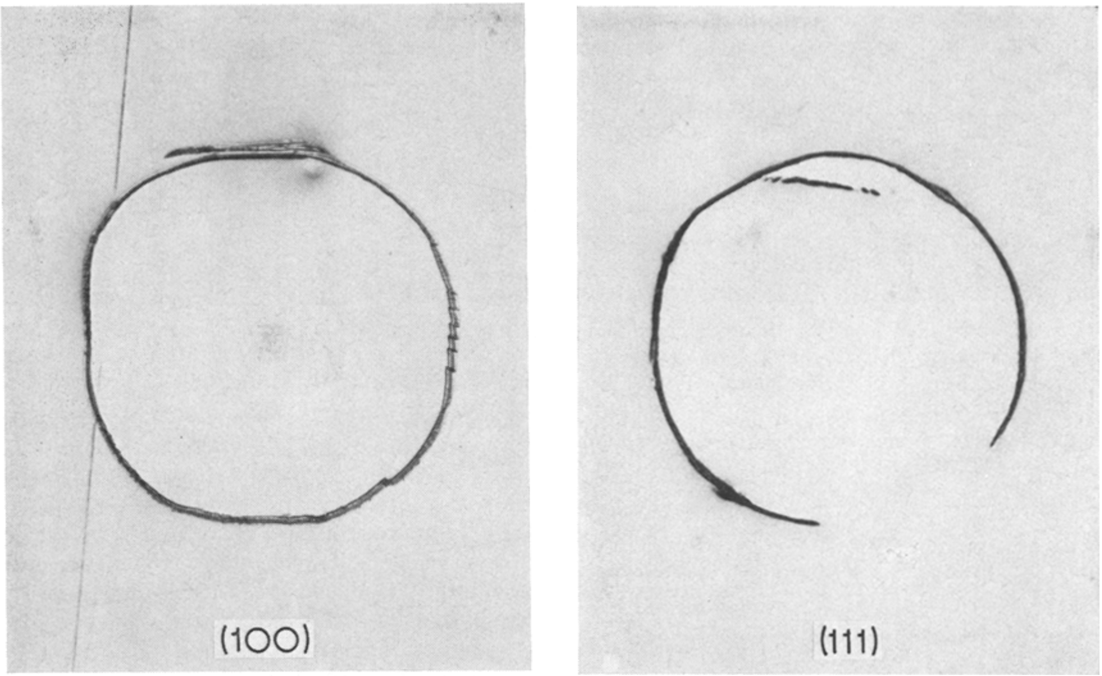

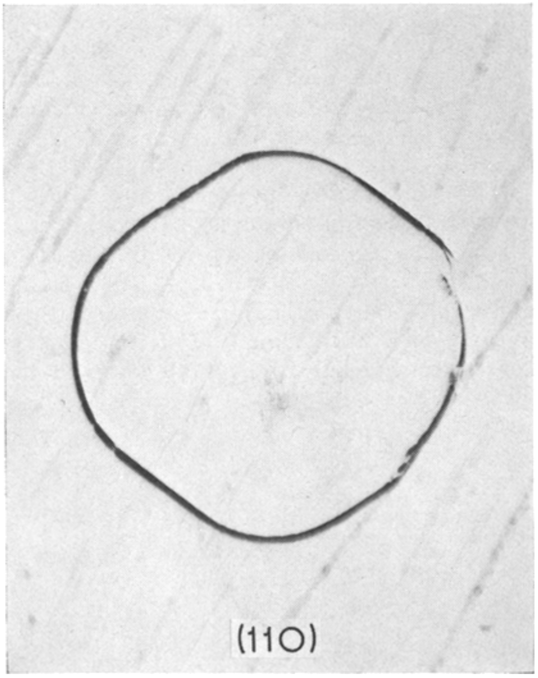

Figure 19 Surface traces of Hertzian cracks on three low-index surfaces of silicon. Specimens indented, etched, and viewed in reflected light. Diameter surface cracks 1.0 mm (After [14].)

on silicate glasses [3, 11, 13, 25-29], quartz [30-33], diamond- [14, 34-39] and zinc blende- [40] structure crystals. Figs. 17 to 19 are selective micrographs from these studies. In Fig. 17 we observe a cone crack in glass, (a) optically from below the specimen at full load, and (b) in profile after a section-and-etch treatment of the unloaded specimen. The isotropy of the system is apparent in this case. In the other two figures, however, the crystalline influence is imposed on the geometry. Here we see an extracted "cone" from an indented quartz slab (Fig. 18), showing the characteristic trigonal symmetry of the (non-centrosymmetric) crystal along the *c*-axis, and etched traces of fractures on three low-index surfaces of silicon (Fig. 19), with the crystal symmetry once more evident. The Hertzian test may be viewed as a simple means of revealing the cleavage tendencies of a given crystal.

As to variants in the cone-crack geometry, we may give brief attention to two interesting examples. In the first (Fig. 20), we show etched crack traces on glass, produced by sliding a sphere across the surface under two different frictional conditions [41]. The circular symmetry of the cone-crack trace is now lost, in approximate accordance with the corresponding stress-trajectory scheme of Fig. 10. In the second example (Fig. 21), we illustrate, via a sequence of section-and-etch profiles in glass, the effect of overloading the indenter [42]: in addition to further extending the developed cone, the

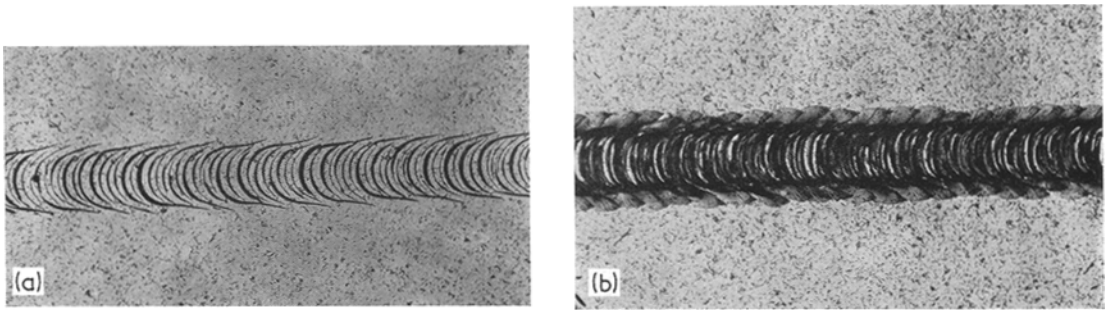

Figure 20 Crack patterns on soda-lime glass produced by sliding tungsten carbide sphere, $r = 1.5$ mm, $P = 10$ N, across surface (from left to right), (a) in *n*-decanol, $f \approx 0.12$, (b) in water, $f \approx 0.44$. Etched surfaces, viewed in transmitted light. Note surface flaws. Width of field 1.25 mm. (Courtesy of G. M. Crimes.)

increasing stress level induces and expands a zone of inelastic deformation immediately below the contact area (where shear and hydrostatic compression are greatest), from which median vent cracks ultimately initiate. We note also in the sequence the tendency to a sideways extension of the cracks with increasing zone size, as with the lateral vents described in the previous subsection; this behaviour, first reported by Culf [27], again points to the existence of a residual stress field. In other words, the sphere effectively "penetrates" the specimen surface at high load, and begins to behave much as a pointed indenter. Indeed, with less brittle solids such as the alkali halide crystals [43], hard metals [44] and PMMA [45], the vent system tends to begin operating before the cone crack has had a chance to develop at all. Finally, we may mention that dynamic loading (Section 2.2.2) and elastic mismatch (Section 2.2.3) can also exert an influence on crack geometry, but these aspects have received relatively little attention in the literature.

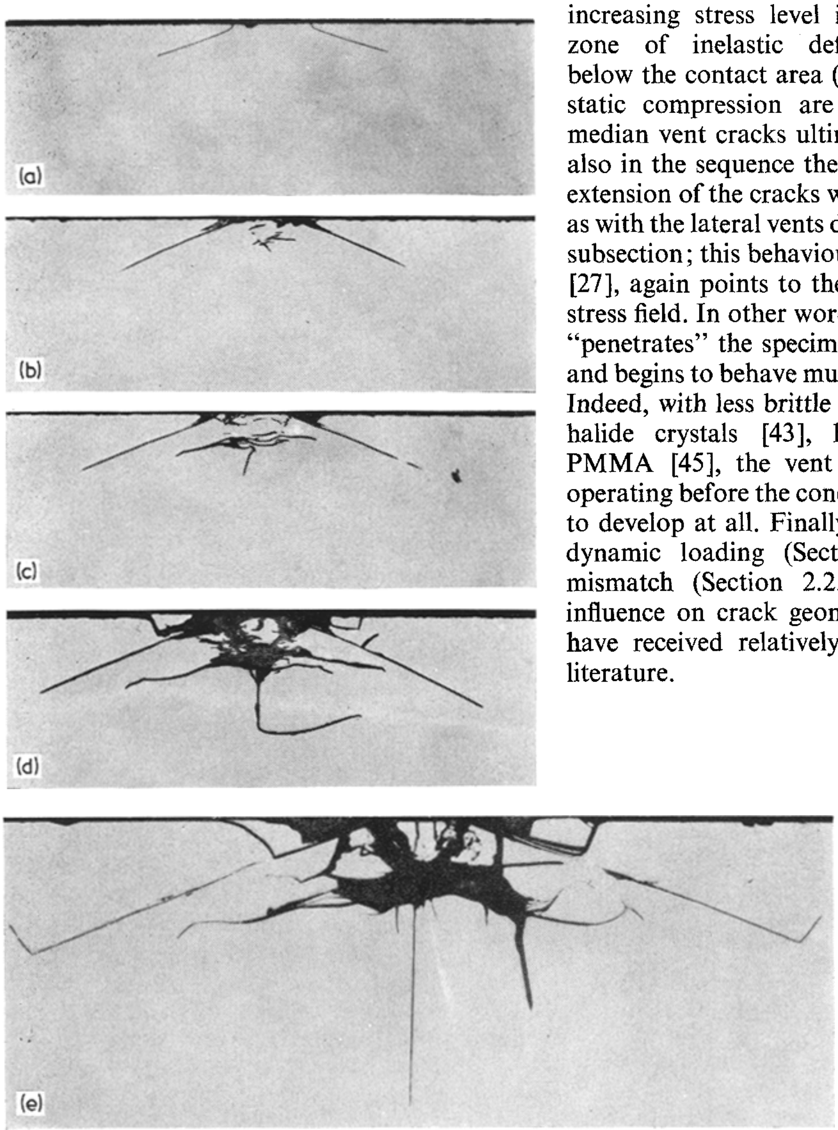

Figure 21 Section-and-etch profiles of crack patterns produced in soda-lime glass by tungsten carbide sphere, $r = 0.5$ mm, at loads (a) 100 N, (b) 140 N, (c) 180 N, (d) 266 N, (e) 500 N. Width of field in (a) to (d) 1.5 mm. Note transformation from characteristic "blunt" to "sharp" indenter patterns with increasing load. (Courtesy K. Phillips.)

3.2. Fracture mechanics

With the elements of indentation fracture geometry established we are in a position to quantify the extent of growth in terms of the important system variables, primarily the applied load, P, and some characteristic crack dimension, say c. The approach used here is that of standard, "linear fracture mechanics" (for a survey, see Ch. 3 of [10]), which essentially provides the mathematical techniques for evaluating the mechanical-energy-release rate function $G = G(P, c)$ (or some equivalent function, such as the so-called "stress-intensity factor") appropriate to a given crack configuration. Unfortunately, exact solutions are unavailable for the complex geometries encountered in indentation problems, and many sweeping approximations have to be made in the analyses.

We must then ask whether the value of G at any given load and crack length is sufficient to drive the crack, i.e. we need a *fracture criterion.* It is not enough to postulate that fracture will occur when the maximum tensile stress in the specimen exceeds some critical level; indeed, such a "critical stress criterion" will *generally* give an incorrect result. Broadly, we may distinguish two basic conditions for crack extension:

(i) *Equilibrium.* In atomistic terms, a brittle crack grows by the sequential rupture of cohesive bonds across the crack plane, thereby creating two new surfaces. At stationary values of U in Equations 17 and 18 the bond-rupture process operates under conditions of thermodynamic (Griffith) equilibrium [4],

$$G = 2\Gamma\,. \tag{19}$$

Then for $G > 2\Gamma$ the crack propagates, in a "dynamic" manner. Equilibrium conditions are most nearly attained at low temperature, high vacuum.

(ii) *Kinetic.* Since the bond-rupture process represents a sequence of *discrete* events, the very real possibility exists of an energy barrier to crack motion at the atomic level. This is manifested by an atomic periodicity in the Γ term, in which case the crack may grow in a rate-dependent manner by thermal fluctuations over the barrier [46]. The crack then propagates according to a "kinetic" equation,

$$v_c = v_c(G)\,, \tag{20}$$

where $v_c(G)$ is a crack-velocity function appropriate to the system under consideration. Kinetic states are most commonly attributable to chemical interactions at the crack tip.

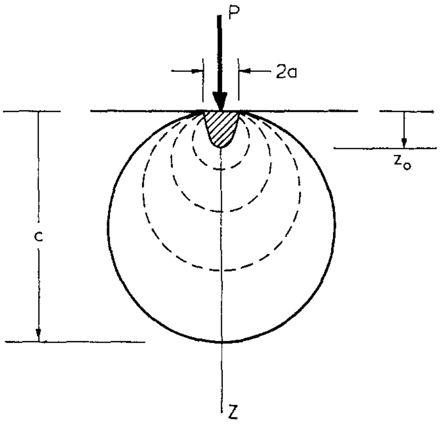

Figure 22 Parameters of the median vent configuration. Broken lines represent stress contours, heavy line represents crack profile, and shading represents inelastic deformation zone.

3.2.1. Sharp indenters – median vent crack (propagation)

Let us consider a well-defined median vent crack, whose depth measured along the z-axis is c at an applied load P. We envisage a small zone of inelastic deformation about the singular point of the indenter as providing a "cut-off depth" z_0 for the tensile field. For analytical purposes it is convenient to model the vent configuration in terms of an internal, penny-shaped crack, as shown in Fig. 22 (cf. Fig. 14). Then the inhomogeneous σ_{22} prior stress field orthogonal to the crack plane may be represented by a family of circular contours with intensity fall-off as the inverse square of the diameter (cf. Fig. 4b). For indenters which conform to the principle of geometrical similarity (Section 2.1), the increase in contact zone with load may be written, in conjunction with Equation 1, as

$$z_0 = \beta a = \beta\left(\frac{P}{\alpha\pi p_0}\right)^{1/2} \approx \left(\frac{\beta^2}{\alpha\pi H}\right)^{1/2} P^{1/2} \tag{21}$$

where β and α are dimensionless geometrical factors determined by zone and indenter respectively. This formulation conveniently introduces the hardness number H into the description. A straightforward fracture-mechanics calculation then gives, for the typical case $c \gg z_0$ (cf. depths of median vent and deformation zone in Fig. 13), [9]

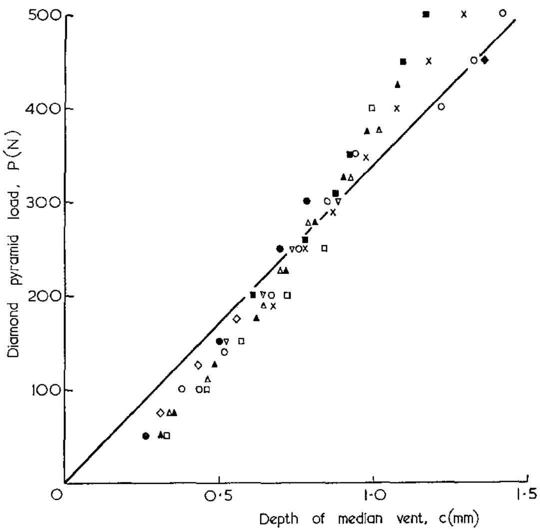

Figure 23 Data from well-behaved median vent cracks in soda-lime glass indented with Vickers pyramid. Each symbol represents a different crack. (After [9].)

$$G = \psi(\nu)\left(\frac{\alpha}{\beta^2}\right)\left(\frac{H}{E}\right)\left(\frac{P}{c}\right), \qquad (22)$$

with $\psi(\nu)$ a dimensionless function of Poisson's ratio; an approximate analysis yields $\psi(\nu) = (1 - \nu^2)(1 - 2\nu)^2/2\pi^4$.

Now if the crack propagates under equilibrium conditions Equation 19 prevails, thus giving

$$\frac{P}{c} = \frac{2\Gamma}{\psi(\nu)}\left(\frac{\beta^2}{\alpha}\right)\left(\frac{E}{H}\right) = \text{const}. \qquad (23)$$

Thus the crack is predicted to grow in a stable manner with increasing load. We plot in Fig. 23 data points from experimental observations of well-behaved vents in Vickers pyramid tests on soda-lime glass [9]: from the slope of the fitted line, in conjunction with the values $\alpha = 2/\pi$ (taking a in Equation 1 as half-diagonal of indentation), $\beta = 2$ (ratio depth/half-diagonal of deformation zone, e.g. Fig. 13), $E = 7 \times 10^{10}$ N m^{-2}, $H = 6.5 \times 10^9$ N m^{-2}, $\Gamma = 4$ J m^{-2} [47], we obtain a calibration constant $\psi = 1.0 \times 10^{-3}$ (glass); this compares favourably with the value $\psi = 1.2 \times 10^{-3}$ computed from the approximate expression above, using $\nu = 0.25$. The theory appears capable of predicting crack depths at least to within an order of magnitude.

There is room for much further study of the vent-crack systems associated with sharp indenters. Micromechanics of the deformation processes which determine the hardness; kinetic effects in the crack propagation; source and nature of the residual stress field responsible for the lateral vents: these are some of the important aspects which remain to be considered.

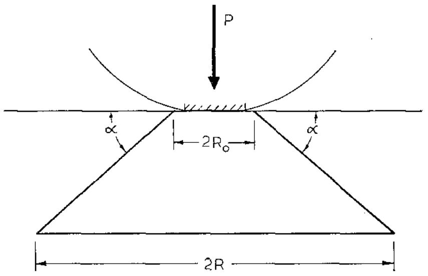

Figure 24 Parameters of the Roesler cone-crack configuration. Indenter contact via machined flat (shaded).

3.2.2. *Indenters with constant elastic contact – cone crack (propagation)*

Let us now consider a well-developed cone crack produced by an indenter with a constant flat (e.g. sphere with segment machined away). The situation is somewhat similar to that of the previous example, in that we may view the tensile field in terms of point-contact loading with a "cut-off" at the cone radius R_0 (Fig. 24); this time, however, the cut-off is determined by an invariant, perfectly elastic contact, so that hardness does not enter the problem. The crack propagates subject to an inhomogeneous σ_{11} prior field, the intensity falling off with distance from the cone apex once more according to an inverse square dependence. This configuration was analysed by Roesler [26], who derived the result

$$G = \frac{\kappa(\nu)P^2}{ER^3}, \; (R \gg R_0) \qquad (24)$$

where $\kappa(\nu)$ is a dimensionless function of Poisson's ratio.

At crack equilibrium we have, combining Equations 24 and 19,

$$\frac{P^2}{R^3} = \frac{2\Gamma E}{\kappa(\nu)}, \; (R \gg R_0)\,\cdot \qquad (25)$$

Fig. 25, in which is plotted data from vacuum tests on soda-lime glass, illustrates the validity of this equation. From the slope of the fitted line, together with the values of Γ and E quoted in the previous subsection, we obtain $\kappa = 1.3 \times 10^{-3}$ (glass); Roesler's numerical analysis of the constant of proportionality in Equation 25 gives $\kappa = 2.75 \times 10^{-3}$ for $\nu = 0.25$.

Also indicated in Fig. 25 is the extent of kinetic crack growth *subsequent* to admitting laboratory atmosphere to the test system, at

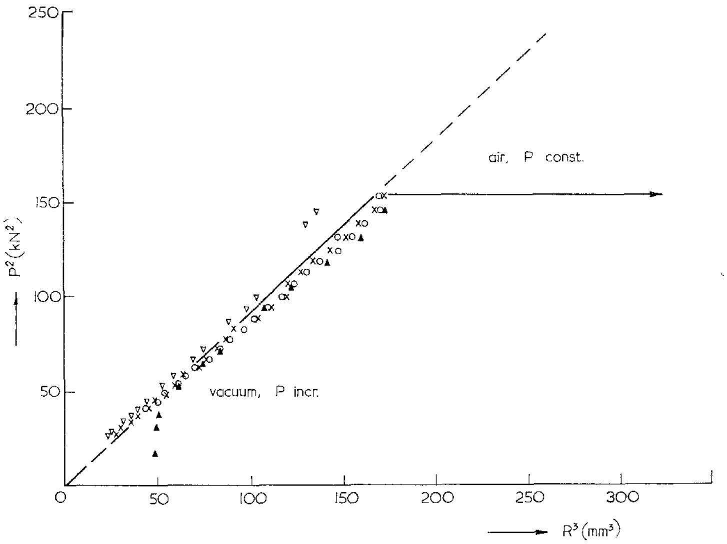

Figure 25 Data from observations of fully-developed cone cracks in soda-lime glass. Plotted points from vacuum tests at variable load, with each symbol representing a different crack. Horizontal arrowed line indicates extent of subsequent cone growth in air at sustained maximum load. (Data courtesy M. V. Swain, R. Starrett, M. Simpson and L. Peters.)

constant load, for 15 min. By observing the time dependence of this stage of growth it is a straightforward matter to evaluate the crack velocity

$$v_c(R) = \frac{\Delta R/\cos\alpha}{\Delta t} \quad (26)$$

(Fig. 24) over a small time interval Δt. Then with $G(R)$ at P = const. in Equation 24 suitably calibrated, the crack-velocity function $v_c(G)$ appropriate to a given test environment is readily plotted [48]. We give greater attention to kinetic aspects of crack growth later in Section 4.3.

3.2.3. Spherical indenters – cone crack (formation)

Thus far in this section we have implicitly assumed the existence of a well-developed crack. We now address the question of how the crack actually forms from an incipient flaw. The cone-crack example is relatively well suited as a case study, because of the degree of control that can be exercised over the flaw characteristics. As we shall see later, a measure of the critical load to cone-crack formation is of value for its implications in many theoretical and practical aspects of brittle fracture.

The conditions which govern the initial stages of cone-crack growth are not easily specified. In general, the starting flaw, effective length c_f, surface location ρ_f, experiences a strongly inhomogeneous, time-varying tensile field as the contact circle expands (Fig. 26). This is illustrated by the plots of the normal stress component $\sigma_{\rho\rho}(z)$ acting on a surface flaw for various contact radii in a typical test configuration (Fig. 27). In such a situation no analysis is feasible without several gross approximations concerning the downward growth of the surface ring crack; these include, a knowledge of the starting point on the surface, ρ_f/a, the assumption that the crack is

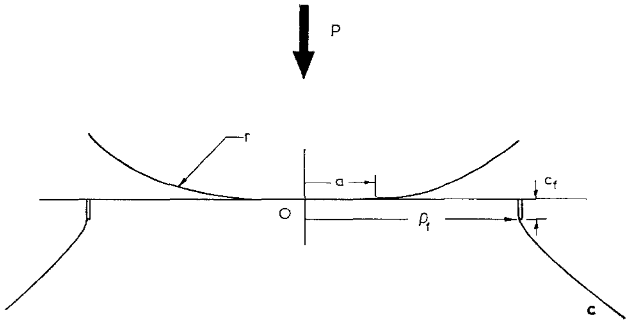

Figure 26 Parameters of Hertzian cone-crack configuration.

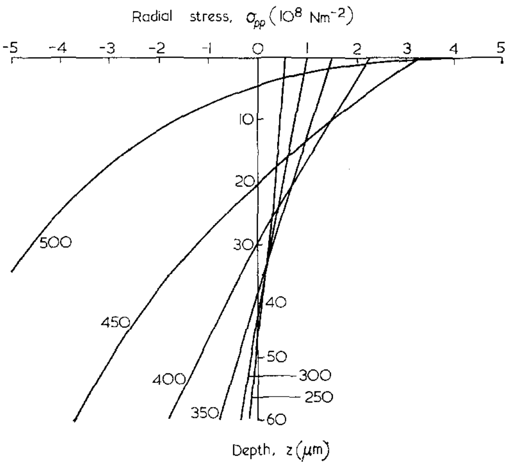

Figure 27 Plots of normal stress $\sigma_{\rho\rho}(z)$ on perpendicular surface flaws in Hertzian field. Calculated for tungsten carbide sphere, $r = 6.35$ mm, on glass, $E = 7.0 \times 10^{10}$ N m^{-2}, $k = 0.55$, flaw location $\rho_f = 500$ μm, at several contact radii a(μm) (labelled). (After [11].)

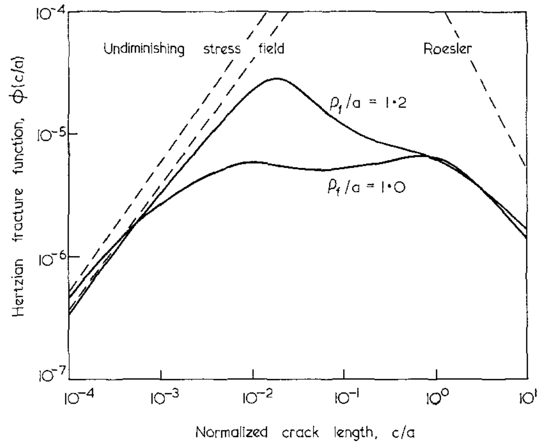

Figure 28 Mechanical-energy-release rate function $\phi(c/a)$ for cone-crack formation. Curves computed for two different starting locations at the specimen surface. Also shown (broken lines) are functions corresponding to small-crack ($c \ll a$) and large-crack ($c \gg a$) approximations. Plotted for $\nu = 0.33$. (After [13, 14, 25, 32].)

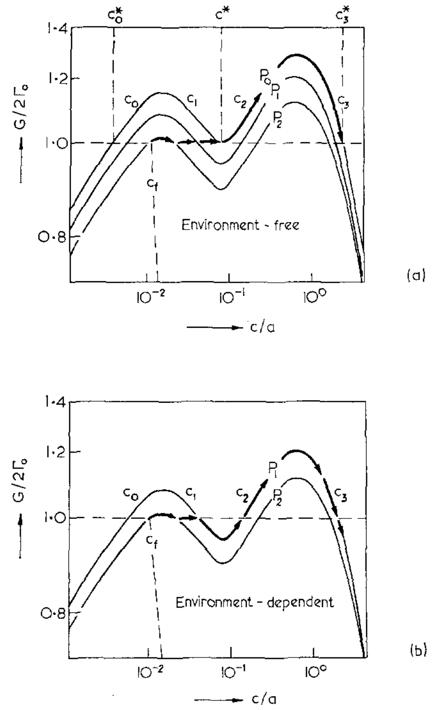

Figure 29 Fracture-mechanics representations for idealized cone-crack formation, at $\nu = 0.33$, $\rho_f/a = 1.0$, under (a) equilibrium, (b) kinetic growth conditions. Heavy, arrowed lines indicate stages of crack extension. (After [49].)

subjected to conditions of plane strain (reasonable for $c \ll a$), the assumption that propagation follows *exactly* the stress trajectory patterns, the assertion that contact friction may be neglected, etc. One then obtains, for isotropic solids, the equation

$$G = \frac{P}{kr}\left[\phi\left(\frac{c}{a}\right)\right]_{\nu, \rho_f/a}. \tag{27}$$

The dimensionless function ϕ is generally evaluated by numerical methods. Fig. 28 shows plots of this function, for $\nu = 0.33$ and two values of ρ_f/a; a "hump" is evident in the $\rho_f/a = 1.0$ curve [13, 14], but is absent in the $\rho_f/a = 1.2$ curve [25, 32]. Also plotted are curves corresponding to a stress field undiminishing from the surface values and to the Roesler expression (Equation 24) for the fully developed cone.

Let us deal with the most interesting, albeit somewhat idealized, case of initiation from the contact circle. We refer to Fig. 29, which represents schematically the formation under both equilibrium and kinetic conditions [49]. In these diagrams the effect of increasing the indenter load is manifested simply as a shift in the curves along the ordinate. The equilibrium requirement, Equation 19, is represented by the horizontal dashed line, and the effective length of the starting ring crack is represented by the near-vertical dashed line (note that since a increases with P, c_f/a at c_f = const. correspondingly decreases). The labels c_0, c_1, c_2 and c_3 designate the four branches of the curve, and the asterisk is used to designate any variable evaluated at the hump crack length c^*.

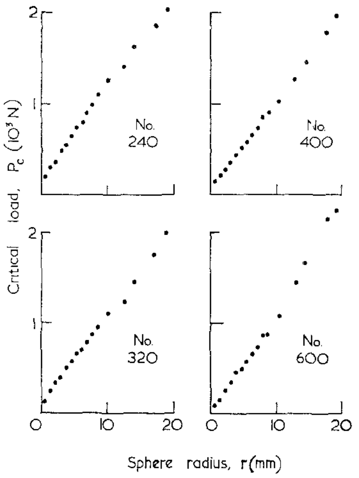

Figure 30 Critical load to cone formation for Hertzian tests on soda-lime glass as function of radius of steel sphere indenter. Surfaces pre-abraded with SiC, different grit sizes as indicated. Each point represents mean of at least ten tests, standard deviation typically $\lesssim 10\%$. (After [53].)

(i) *Equilibrium:* test conditions such that the fracture-surface energy is given by its environment-free value Γ_0. We consider first a starting flaw such that the line c_f = const. intersects the line $G = 2\Gamma_0$ in Fig. 29a within the size range $c_0^* \leqslant c_f \leqslant c^*$. Upon loading, the crack system proceeds to this intersection point, at $P = P_2$, whence downward growth occurs spontaneously from the c_0 to the c_1 branch. Further, stable extension of the surface ring from the c_1 to the c_2 branch ensues as the load continues to increase. At $P = P_0^*$, where c_1 and c_2 merge at c^*, the ring propagates spontaneously into the full cone, at c_3^*; typically, $c^* \approx 50$ µm, $c_3^* \approx 500$ µm. It is this final, unstable stage which is observed in the Hertzian test, and the condition for its occurrence may be written as $c = c^* \approx a/10, P = P_0^*$; Equations 27 and 19 combine to give the critical load

$$P_c = P_0^* = \frac{2\Gamma_0 kr}{[\phi(c^*/a)]_{\nu,\rho_f/a=1}}, \quad (c_0^* \leqslant c_f \leqslant c^*). \quad (28)$$

The result $P_c \propto r$ expresses formally the long-standing "Auerbach's law", discovered empirically by Auerbach in 1891 [50] and the subject of much contention ever since (for an historical resumé up to 1956, see papers by Roesler [51] and Tillet [52]). We may note that, taken in conjunction with Equations 1, 4 and 7, Auerbach's law implies that the maximum tensile stress in the specimen at cone fracture is size-dependent, $\sigma_{\rho\rho}(\rho_f/a = 1) \propto r^{-1/3}$; in other words, the "critical-stress criterion" is violated. This may be seen as a consequence of the flaw having to overcome an *energy barrier* to growth (via the hump), much as the Stroh-type pile-up microcracks evident in semi-brittle solids (see Ch. 2, [10]).

Definitive experiments confirming the validity of Equation 28 have been performed on abraded glass surfaces, under both constant displacement rate and impact loading conditions (Section 2.2.2), by Langitan and Lawn [53]. Fig. 30 shows some of the data, for four different severities of surface abrasion. In accordance with the predictions of Equation 28, Auerbach's law is found to be obeyed over the range of indenter size studied, with a value of calibration constant, for $\Gamma_0 = 4$ J m^{-2} and $k = 0.55$ (tungsten carbide sphere on glass), of $\phi^* = 5 \times 10^{-5}$ (glass) *independent of flaw size*; this value compares with that computed theoretically, $\phi^* = 5 \times 10^{-6}$ ($\nu = 0.33, \rho_c/a = 1.0$) [14]. Among the solids other than glass in which this law has been verified experimentally, are included diamond [54], silicon [14], vitreous carbon [55] and titanium carbide [56].

Now suppose the line c_f = const. to intersect the $G = 2\Gamma_0$ level within the size range $c_f \ll c_0^*$ (not represented in Fig. 29a). In this case the surface ring propagates directly from the c_0 to the c_3 branch, i.e. there is no energy barrier to cone formation. The fracture condition therefore becomes $c = c_f = c_0, P = P(G = 2\Gamma_0) > P_0^*$. Since for small flaws the computed $G(c/a)$ curve is asymptotic to that for an undiminishing stress field (Fig. 28), $\phi(c_f/a)$ may be evaluated in terms of conventional uniform tension formulae. We accordingly obtain, after some manipulation,

$$P_c = \frac{\Gamma_0^{3/2} k^2 r^2}{\chi(\nu) E^{1/2} c_f^{3/2}}, \quad (c_f \ll c_0^*, \rho_f = a), \quad (29a)$$

where

$$\chi(\nu) = \left\{\frac{3}{4}\,[3(1 - 2\nu)^2 (1 - \nu^2)/32\pi]^3\right\}^{1/2}$$

is a dimensionless constant.

The transition between the extremes of Equations 28 and 29 as c_f diminishes below c_0^* has been discussed elsewhere [52, 53].

(ii) *Kinetic:* test conditions such that the system proceeds in a rate-dependent manner toward a

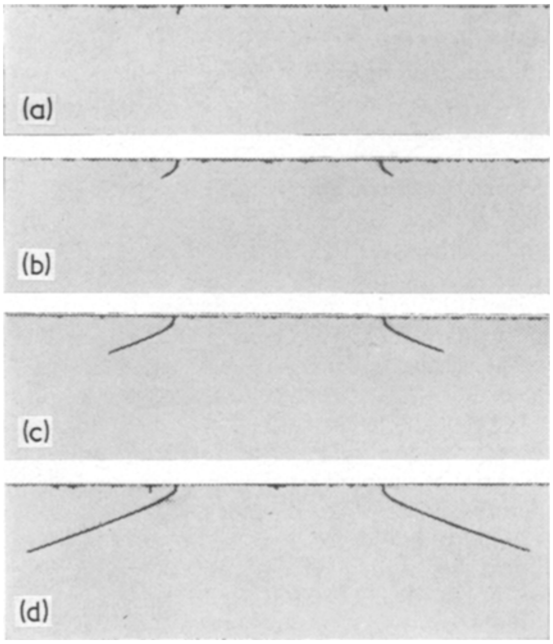

Figure 31 Section-and-etch sequence of Hertzian cone-crack growth in soda-lime glass in air. Load durations, (a) 0.5 sec, (b) 1.4 sec, (c) 1.7 sec, and (d) 100 sec. Note growth of "embryo" crack in (a) and (b) prior to sudden full development in (c) and (d). Width of surface ring crack 0.86 mm. (After [24].)

reduced, environment-dependent fracture-surface energy, $\Gamma < \Gamma_0$. We consider the case depicted in Fig. 29b, in which the indenter is loaded "instantaneously" to $P = P_1 < P_0{}^*$ and is subsequently maintained at this load for a critical duration, t_c, to cone fracture. Arrival at the c_1 branch is exactly as for the equilibrium case in Fig. 29a, but growth thereafter to the c_2 branch, thence to the cone at c_3, occurs by "tunnelling" through the hump. Fig. 31, a sequence of section-and-etch profiles, illustrates the various stages of kinetic growth in soda-lime glass for tests in laboratory (moist) air [24]. Then the critical condition for cone fracture may be specified as

$$P_c = P_1 < P_0{}^* \,, \; t_c = \int_{c_f}^{c_3} \frac{dc}{v_c(c)} \,, \qquad (30)$$

where the times spent in dynamic growth ($c_0 \rightarrow c_1$, $c_2 \rightarrow c_3$) may generally be disregarded.

This aspect of cone-crack formation is very difficult to quantify in terms of the Hertzian test parameters. Moreover, we have considered only the simplest of loading modes, $P_1 = \text{const.}$ (see Section 2.2.2), in the representation of Fig. 29b. Reference is made to the paper by Langitan and Lawn [57] for further discussion.

Despite the inadequacies in the treatment above, the basic results obtained establish a sound basis for the application of Hertzian fracture testing to many facets of brittle cracking. Equation 28 offers itself as an avenue to simple and rapid fracture-surface energy investigations, without the need for stringent specimen preparation; Equation 29 provides the means for sampling the flaw distributions and micro-strength variations over the specimen surface; and Equation 30 provides a useful guide to the magnitude of kinetic effects, in that it "averages" the crack velocities at any specified load level. On the other hand, it needs to be recognized that small changes in the contact conditions can lead to substantial deviations from idealized behaviour. For example, we recall in Fig. 28 the dramatic change in position and form of the $G(c/a)$ curve in going from $\rho_f/a = 1.0$ to 1.2; the more remote starting location does in fact accord with experimental fact. This and a similarly dramatic sensitivity to variations in Poisson's ratio have been discussed by Wilshaw [25], whose analysis indicates a simple generalization of Equation 29a in the small-flaw régime

$$\begin{aligned} P_c &= \frac{\Gamma_0{}^{3/2} k^2 r^2}{\chi(\nu) E^{1/2} c_f{}^{3/2}} \left(\frac{\rho_f}{a}\right)^6 \\ &= \left(\frac{2\pi}{1-2\nu}\right) \rho_f{}^2 \sigma_T \,, \;\; (c_f \ll c_0{}^*, \rho_f \geqslant a) \qquad (29b) \end{aligned}$$

where the tensile strength σ_T is introduced via Equations 1 and 7 by equating to $\sigma_{\rho\rho}$, but which is limited to a numerical treatment of the corresponding effect on Equation 28. The principal difficulty here is that the formation stage of cone fracture takes place in the very near-contact region most susceptible to details in the test conditions. Even the resources of the high-speed computer appear to be limited in their ability to deal with the more complex cases encountered in normal practice [11].

4. Measurement of fracture parameters

The broad aim of brittle fracture testing is to investigate the role of various material properties in the determination of strength. This is most conveniently achieved through the evaluation of such fracture parameters as fracture-surface energy, crack-velocity function constants and flaw-distribution factors. Indentation techniques are useful here, with many immediate practical advantages over more conventional test arrangements: these advantages include; *economy* in material and time (the accumulation of some hundreds of results within an interval of hours from a surface about 25mm × 25mm being typical); *reproducibility* of results (provided some control can be exercised over the size of the initiating flaw), with the possibility of performing several tests on the one surface under a variety of test conditions; *simplicity* in experimentation, requiring in the simplest applications the availability of standard testing machines; capacity to *probe* an inhomogeneous surface for microstrength variations. Balanced against these advantages is one major limitation: because of a general inability to accommodate exact details of the complex, inhomogeneous indentation fields within the fracture-mechanics analyses, the constants of proportionality in the predicted fracture equations are subject to considerable uncertainty (typically a factor of two, but up to an order of magnitude in unfavourable cases, as the analyses of Section 3.2 indicate); nevertheless, while *absolute* determinations of the fracture parameters may not be reliable, *relative* determinations can be performed with an accuracy which compares favourably with most conventional fracture techniques.

4.1. Experimental considerations

Since the conditions of testing can have a large influence on indentation fracture behaviour, we outline briefly some of the more important aspects of the experimental arrangements in general usage:

(i) *Material preparation.* The mechanical state of any material will depend in some complex way on its past history; the *bulk* state will tend to be reflected in those parameters which relate to crack *propagation*, while the *surface* state will reflect more in those parameters which relate to crack *initiation.* Microstructure, degree of surface damage, distribution of residual stresses, etc., will be strongly affected by the processes of fabrication, shaping and finishing. Most important is the need to pay attention to surface preparation of test specimens, according to the property under investigation. In those cone-crack tests which require the presence of a uniform density of surface flaws, it is convenient to subject the specimen to a controlled abrasion treatment [53]. On the other hand, if it is the distribution of incipient flaws on pristine or as-received surfaces which is itself the subject of study, no surface preparation (other than careful cleaning) is required at all. At the other extreme, where crack initiation at the surface is to be discouraged, as with the study of vent cracks, an annealing or chemical-polishing treatment may be of advantage.

(ii) *Test environment.* The nature of the test surrounds can have a considerable effect on the indentation fracture pattern, principally in determining whether crack growth occurs under equilibrium or kinetic conditions. The chemical concentration of reactive species available to the crack tip (including species pre-present *within* the solid) and the temperature constitute the most important variables. A systematic investigation of these variables requires the facility of an environmental chamber [15].

(iii) *Loading mode.* For any test in which kinetic processes are involved it is necessary to be aware of load-rate effects. In Hertzian tests, for example, the influence of loading mode will be felt most strongly when the velocities of contact, $\dot{a}$ (Section 2.2.2), and crack propagation, $v_c = \dot{c}$ (Equation 20), are of comparable magnitude [11]. In practice, a very wide range of load rates can be covered by appropriate changes in mode (see Fig. 8).

(iv) *Observation and detection of cracks.* In transparent solids the progress of crack growth can usually be followed *in situ* by straightforward optical techniques. Opaque solids pose a greater problem: in those tests where only the *onset* of fracture needs to be recorded (e.g. Section 3.2.3), acoustic sensors may be used to detect the accelerating crack [58]; where the crack front has to be followed throughout the entire test (Sections 3.2.1 and 3.2.2), however, it is usually only possible to extract quantitative information by examining the specimen *after* indentation, e.g. by the section-and-etch method (Fig. 31) [24], although direct observations have been made in special cases in which the crack intersects the specimen surface [23].

4.2. Fracture-surface energies

4.2.1. Absolute determinations

We have already pointed out the uncertainties involved in most calculations of the extent of indentation cracking. In all cases studied in Section 3.2 the fracture condition derived involves a proportionality constant which is a (usually sensitive) function of Poisson's ratio

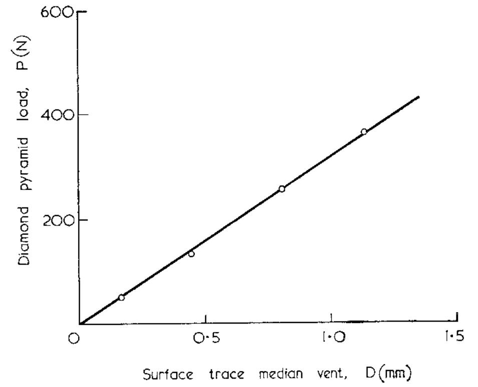

Figure 32 Data from surface traces of median vent cracks on a polished surface of WC/0.06 Co cemented carbide indented with a Vickers pyramid. Here $D \approx c$ (see Fig. 15a). (After [61].)

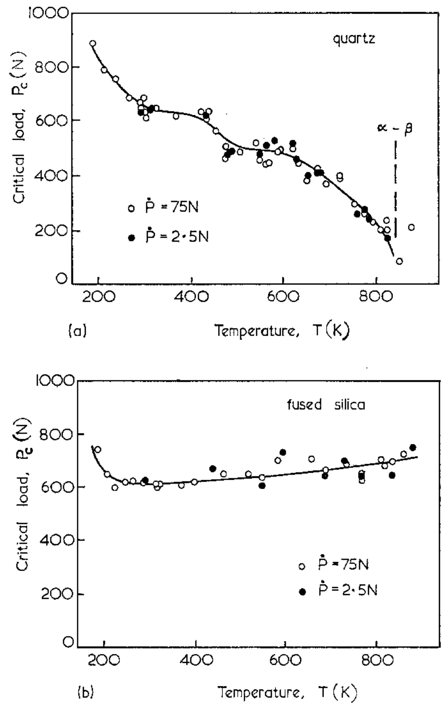

Figure 33 Critical load to cone formation for Hertzian tests on (a) quartz, (b) fused silica, as function of temperature. Vacuum data, r = 6.35 mm (WC). Surface pre-abraded with no. 500 grit. Each point mean of at least ten tests, standard deviation typically $\lesssim$ 10%. (After [62].)

(and sometimes of other factors as well). Thus not only is the absolute fracture energy measured for any specific material subject to large systematic error, but comparative measurements on different materials tested under identical conditions cannot be taken as a reliable indicator of relative values.

With these reservations in mind we proceed to a crude analysis of Hertzian fracture data. Typically, for highly brittle solids, the critical load to cone formation within the Auerbach range measures at $P_c/r \approx 10^5$ N m^{-1} (e.g. see Fig. 30, and later, Fig. 33); with $k \approx 0.5, \phi^* = 5 \times 10^{-6}$ (computed value at $\nu = 0.33$, $p_c/a = 1.0$, Section 3.2.3.), Equation 28 gives $\Gamma \approx 0.5$ J m^{-2}, which is just about the correct order of magnitude. Similar estimates of the fracture surface energy can be obtained from measurements of the fully developed cone (Section 3.2.2).

An interesting extension of the procedure, particularly to less brittle, opaque materials, can be made to the case where median vents beneath a sharp indenter break through to the specimen surface, as in the schematic representation of Fig. 15a. Then the surface trace gives a measure of the depth of the vent. Palmqvist [59, 60], using the Vickers pyramid test on hard metal surfaces, was the first to adapt the surface crack pattern to an assessment of fracture toughness; with empirical insight, he was able to identify the most important variables, especially hardness. The analysis of Section 3.2.1 provides a sound theoretical justification of Palmqvist's method. To illustrate the approach, we refer to Vickers indentation data for tungsten carbide in Fig. 32 [61]: from the slope of the fitted straight line, along with $\alpha = 2/\pi$, $\beta = 2$ (as in Section 3.2.1), $E = 4 \times 10^{11}$ N m^{-2}, $H_V = 2 \times 10^{10}$ N m^{-2}, and $\psi = 1.2 \times 10^{-3}$ (computed value, for $\nu = 0.25$), Equation 23 yields $\Gamma \approx 3$ J m^{-2} as a crude estimate of the fracture surface energy. The full potential of this method as a quantitative tool for measuring effects of surface treatments on fracture resistance [61], the energies of interfaces (such as grain boundaries) outcropping the specimen surface, etc., has yet to be realized.

4.2.2. Temperature variations – comparative tests on silica

A particularly useful application of indentation testing in brittle solids is in the investigation of the temperature dependence of fracture-surface energies. A striking example is provided by Swain *et al.* in an extensive study of the fracture properties of various modifications of silica, SiO_2 [62]. Fig. 33 shows some data for fused silica and quartz tested under vacuum conditions and within the Auerbach range, with the critical load to cone fracture $P_c(T)$ plotted over the temperature range T = 200 to 900 K. Both these structural modifications are characterized by a strong -Si-O-Si- linkage, but differ in the manner of stacking of SiO_4^{4-} tetrahedral units; in the amorphous fused silica modification the stacking is disordered, while in the crystalline quartz modification it is ordered. The divergent behaviour in Fig. 33 must be sought in the structural *differences* rather than *similarities*, which points to the stacking. It is suggested [62] that the key to the dramatic plunge in the fracture-surface energy for quartz on approaching the temperature 846 K, where the structure undergoes a second-order $\alpha \rightarrow \beta$ phase transition, is associated with a cooperative increase in amplitude of the vibrational modes of the tetrahedra, thereby elongating the -Si-O-Si- linkage to near-breakage point. No such thermal anomalies are evident in fused silica, the disorder in the vibrational modes being virtually complete at all temperatures.

Apart from affording valuable clues to the fracture behaviour of brittle solids at the fundamental, atomic level, the results in Fig. 33 serve also to emphasize the economy of the Hertzian test. Each data point represents the mean of at least ten tests - the accumulation of a comparable quantity of information from conventional testing techniques would be a formidable task indeed.

4.2.3. *Microstructural variations - glass ceramics*

Many materials suffer microstructural changes when subjected to certain treatments in their preparation. This is especially so of glass ceramics, whose mechanical properties may be controlled to some extent by suitable heat-treatments. Indentation techniques may be usefully applied to measure any attendant changes in the fracture energy, provided the scale of the microstructure remains small in comparison with that of the crack system. In Hertzian testing, for instance, one avoids the complication of accounting for the possible role of variable microstructural flaws in cone-crack initiation by introducing abrasion damage of relatively high severity; this tends to impose an upper limit of about one micron on the scale of structural detail that can be accommodated in practice.

Investigations along these lines are in their infancy, but work on two glass ceramic systems [63, 64] does indicate that the Hertzian method may be of great value in nondestructively assessing the temperature dependence of strengthening mechanisms in this class of material.

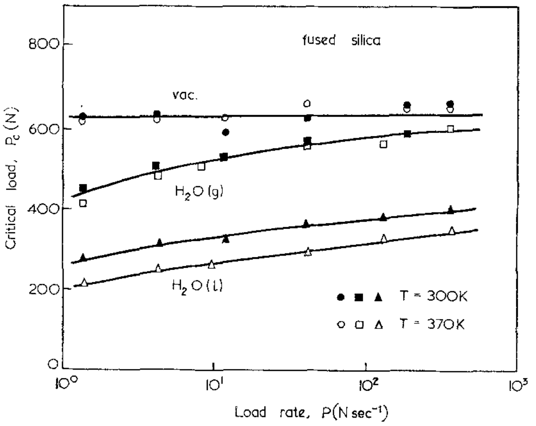

Figure 34 Critical load to cone formation for Hertzian tests on fused silica as function of load rate. $r = 6.35$ mm (WC). Surface pre-abraded with no. 500 grit. Vacuum and water environments at two temperatures. (Pressure in water vapour environment 260 N m^{-2}.) Each point mean of at least ten tests, standard deviation typically $\lesssim 10\%$. (After [62].)

4.3. Kinetic effects

4.3.1. *Semi-quantitative investigations - Hertzian tests on SiO_2/H_2O system*

Another aspect of fracture testing which lends itself to investigation by indentation methods is that of rate-dependent crack propagation. The Hertzian test is again of unique value in systematically following the effects of a large number of likely variables, although as indicated in Section 3.2.3 a quantitative evaluation of specific kinetic parameters from the data is not feasible by this method. Most commonly, the indenter is loaded in either the constant $\dot{P}$ or $\dot{Z}$ mode (Section 2.2.2), and the "magnitude" of the kinetic effect is measured in terms of the depression in critical load with respect to the vacuum value.

The only fracture system studied in depth in the context of kinetic behaviour is that of silica/water and its variants. Basically, the water molecules hydrolyse the crack-tip siloxane bridging bonds according to a rate-dependent reaction,

$$\begin{aligned}&(\text{H-O-H}) + (\text{-Si-O-Si-})\\&\qquad \rightarrow (\text{-Si-OH . HO-Si-}), \qquad (31)\end{aligned}$$

to form terminal hydroxyl groups. Fig. 34 demonstrates the time dependence of the fracture

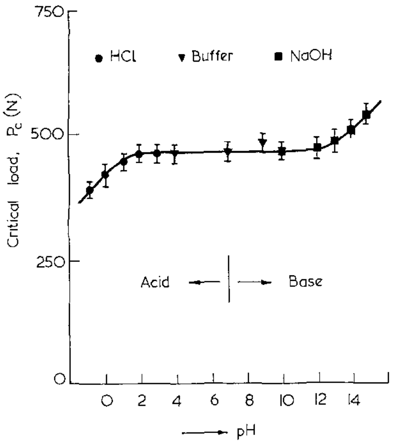

Figure 35 Critical load to cone formation for Hertzian tests on soda-lime glass as function of pH of aqueous solution. r = 6.35 mm (steel). Surface pre-abraded with no. 400 grit. Instron data, cross-head speed 0.2 mm min^{-1}. Each point mean of at least ten tests, standard deviation indicated. (After [57].)

load to be most strongly affected at low load rates, high chemical concentrations, and high temperatures; from these limited observations it is possible to deduce a great deal about the actual sequence of mechanisms by which the water molecules are first transported to and subsequently interact with the crack-tip structure [62].

Some of the variants have been discussed by Langitan and Lawn [57]. One example is shown in Fig. 35 for tests at fixed displacement rate on soda-lime glass in aqueous solutions of varying pH. The kinetic fracture is clearly enhanced by a greater acidity.

A different type of kinetic fracture process has been observed in irradiated quartz [65]. Protons injected into the lattice are able to diffuse internally to the crack tip, and to interact there in a manner somewhat analogous to that depicted by Equation 31. In this case time-dependent Hertzian fracture occurs even under vacuum conditions.

4.3.2. Crack-velocity functions

For a more quantitative evaluation of kinetic fracture parameters it is necessary to go to configurations which provide the means for a direct measure of the crack velocity. The most suitable indentation technique for this purpose would seem to be that involving the well-developed cone crack (Section 3.2.2). Through the Roesler formula, Equation 24, one may investigate the function $v_c(G)$ under any specified test condition. Both Roesler [26] and Culf [27], the founders of the technique, gave adequate demonstrations of the ability of the cone crack to respond to reactive environments with time, although neither addressed the explicit problem of the crack-velocity behaviour.

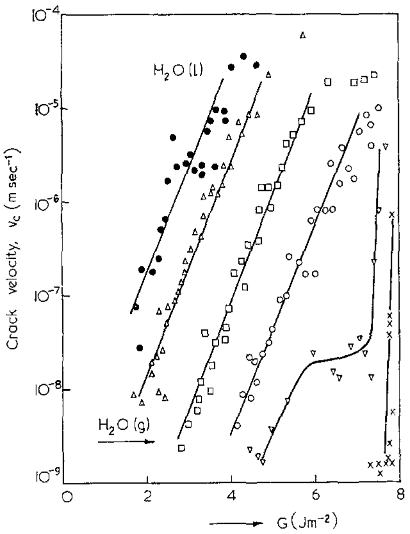

Figure 36 Crack velocity as function of mechanical-energy-release rate for cone-crack tests on soda-lime glass in water environments. Radius of contact flat 1.0 mm. Closed symbol denotes liquid; open symbols denote vapour, pressure (N m^{-2}) 2 × 10^{3} (△), 1 × 10^{2} (□), 10 (○), 1 × 10^{-2} (▽), 1 × 10^{-4} (×). (After [48].)

Recent developments along these lines have been described for soda-lime glass in water environments [48]. The results are plotted in Fig. 36, in which the calibrated constant $\kappa = 1.3 \times 10^{-3}$ in Section 3.2.2 has been used to compute the G values in Equation 24. It is seen that the crack velocity is exponentially dependent on the crack driving force over a significant portion of the plot, a result which accords with theoretical predictions based on reaction-rate theory [46]. From curve-fits to the data one may derive compact, semi-empirical crack-velocity equations in terms of the important test variables outlined in the previous subsection. Such equations are of extreme importance in characterizing the "static fatigue" behaviour of brittle materials [66].

4.4. Flaw statistics

As remarked earlier, the nature and origin of flaws in brittle solids are not very well understood. It is known that surface microcracks are introduced into surfaces by contact damage caused by minute particles, such as dust in the atmosphere, but many other potential sources exist in most materials (see [10], Ch. 2, for a survey). Physical observations of such flaws, especially during their evolution, are not generally possible, although some workers have shed a little light on intrinsic damage processes using microindentation techniques [67, 68].

A typical surface exposed to an everyday environment would, therefore, be expected to accumulate throughout its history a wide distribution (in both size and location) of these flaws. Then the Hertzian fracture equation (Equation 29b) may be conveniently applied to determine the size of the critical flaw for cone formation within any pre-selected region of the surface, *provided* the condition $c_f \ll c_0^*$ is not violated. From a series of probes of this type one may compile a flaw count for any specified size range, and thereby establish the distribution. Two approaches to this end have been described in the literature:

(i) *Direct approach* [69-71]. An estimate of the densities of surface flaws as a function of size may be obtained directly by dividing the flaw count, $n(c_f)$, by the sum of areas, $A_i(c_f)$, "searched" by the indenter [71],

$$\lambda(c_f) = \frac{n(c_f)}{\sum_{i=1}^{N} A_i(c_f)}, \quad (N \text{ indentations}) \qquad (32)$$

(c_f is taken as the mid-range value of a small interval of sizes). The area A_i is defined for an indenter load P_i as that within which a flaw c_f would have propagated to cone fracture (this definition does not necessarily require that fracture should actually occur). At (and below) some minimum load level, corresponding to a tensile stress at the contact circle just sufficient to satisfy Equation 29b, the searched area is zero, whereupon at higher loads it grows as an ever-expanding annulus. A histogram of flaw densities computed in this way from test data on an as-received glass surface is presented in Fig. 37.

In principle, one should be able to extend this approach to the exploration of flaw locations as well as sizes; this would be of value in evaluating *size effects* in the strength of materials. However, the accumulation of adequate quantities of data for a statistically significant analysis would be a formidable task indeed.

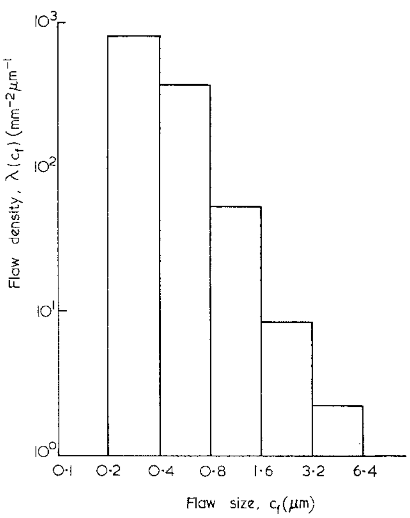

Figure 37 Histogram showing flaw density as function of flaw size for as-received plate glass. Results from 99 Hertzian tests, WC ball $r = 0.35$ mm. (After [71].)

(ii) *Empirical approach* [72-74]. Based on probability theory, this alternative approach begins with the tacit assumption that the flaws comply with some standard distribution law. The idea is to curve-fit the pre-supposed distribution function to the experimental data, and thereby evaluate characteristic strength parameters for the surface. A good deal of attention has been devoted to this approach in the literature, largely because of the demand for simple, empirical, strength equations in engineering design. However, such exercises in statistical data manipulation offer no physical insight into the flaw problem, and we accordingly leave the interested reader to pursue the topic further in the original reference sources.

5. Practical applications

We are now in a position to indicate how knowledge of indentation fracture behaviour may be applied to the study of a wide variety of technological problems. In the simplest applications the indenter can be regarded as a tool for systematically "sampling" variations in mechanical response over a given test surface. At the other end of the spectrum the indentation test may be taken to simulate individual events in multi-stage stochastic microfracture phenomena, and thus to provide the starting point for a crude working model. Comprehensive, definitive studies along these lines are as yet lacking, largely because of the gross complexity which besets "real systems". In this final section we attempt merely to give a brief account of a few selected areas where some progress has been made.

5.1. Surface strength measurements

The maximum homogeneous tensile stress which a material can sustain prior to catastrophic fracture is a quantity of considerable importance as a design parameter in engineering applications. For a given specimen the so-called "tensile strength", σ_T, accordingly constitutes a figure of merit which depends on many of the more fundamental fracture properties described in the previous section. We have already pointed out in deriving Equation 29b (see Section 3.2.3) the relation between this quantity and the Hertzian fracture load, P_c, and location, ρ_f, in the limit of small flaws ($c_f \ll c_0{}^*$, i.e. flaw sufficiently small that the tensile stress distribution along its length is effectively uniform). It is to be appreciated, however, that measurements of P_c and ρ_f alone tell us nothing as to the extent to which changes in σ_T may be attributed to separate effects on flaw size, fracture surface energy, or Poisson's ratio [via $\chi(\nu)$]. Moreover, it will be recalled that Equation 29b pertains to equilibrium conditions of crack growth, and to a somewhat idealized Hertzian stress field situation; the influence of environmental effects, frictional tractions at the contact interface, etc., must be taken into account in any complete analysis.

A particularly useful application of the indentation fracture approach is to the detection and measurement of residual stresses in a treated surface. In simple terms, the difference in fracture behaviour between treated and untreated (or annealed) surfaces may, under otherwise identical test conditions, be taken as an indication of the magnitude of the residual stress component. As a qualitative example, we show in Fig. 38 the variation of the critical load to Hertzian cone formation with duration of an ion-exchange treatment in soda-lime glass [75]. The treatment consisted of immersion in a molten potassium nitrate bath at 643 K. The results in the figure reflect the kinetics of the ion-exchange process: the initial rapid increase in P_c is considered to arise from residual compressive stresses as the K^+ replace the smaller Na^+ ions in the near-surface of the glass, and the subsequent drop-off from relaxation of these stresses as the ions gradually diffuse into the structure to low-energy sites [75].

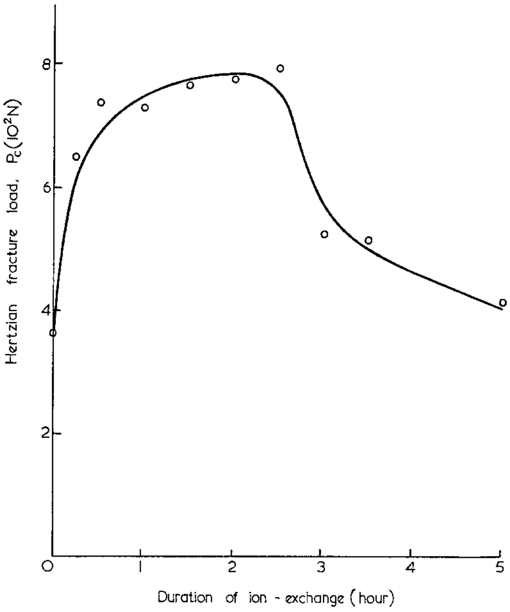

Figure 38 Critical load to cone formation for Hertzian tests on unabraded soda-lime glass surfaces as function of duration of ion-exchange treatment. Instron data at S.T.P., r = 1.0 mm (WC). (Courtesy S. J. Bloomer.)

A second study, on thermally toughened glass plates, illustrates how one may extract more quantitative information on the residual surface stress, σ_R, from such measurements [76]. One compares Hertzian fracture results obtained on the glass in its toughened ($\sigma_R \neq 0$) and annealed ($\sigma_R = 0$) states; Equation 29b for the two states then modifies simply (by the principle of superposition) to

$$\left.\begin{aligned} \sigma_T &= \left(\frac{1-2\nu}{2\pi}\right)\left(\frac{P_c}{\rho_f{}^2}\right)_{\sigma_R=0} && \text{(annealed)} \\ \sigma_T{}' &= \left(\frac{1-2\nu}{2\pi}\right)\left(\frac{P_c}{\rho_f{}^2}\right)_{\sigma_R\neq 0} = \sigma_T - \sigma_R && \text{(toughened)} \end{aligned}\right\} . \quad (33)$$

On glass surfaces abraded with no. 1000 SiC grit, it is found that $\sigma_T = (196 \pm 16)$ MN m^{-2} and $\sigma_T{}' = (317 \pm 23)$ MN m^{-2} (mean ten tests $\pm$ standard deviation), thus giving $\sigma_R = -(121 \pm 39)$ MN m^{-2}. This compares favourably with the value $\sigma_R = -(122 \pm 4)$ MN m^{-2} determined independently by optical means. Of course, the Hertzian result is an averaged value over the length of the surface flaws ($c_f \approx 1$ µm in the present case), and accordingly provides no

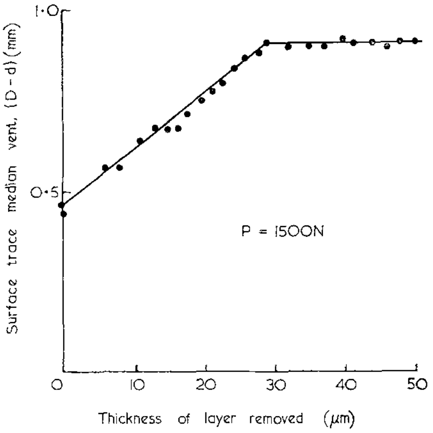

Figure 39 Data from surface traces of median vent cracks in WC/0.06 Co cemented carbide indented with a Vickers pyramid, showing variation of crack length (D = distance between extremities of traces, d = diagonal indent) with depth of material polished away from an originally ground surface. (After [61].)

insight into the *gradient* in residual stress below the specimen surface.

A final illustration of the approach, taken from an investigation by Exner on hard metal surfaces using a Vickers pyramid indenter [61], is given here. Starting with a ground surface, indenting at a prescribed load, and then successively polishing away and re-indenting the surface, he obtained the crack length data shown in Fig. 39. The plot indicates a residual compressive stress, associated with the original grinding damage, extending to a depth $\approx$ 30 μm. This procedure thus complements that outlined in the previous paragraph.

Other reported surface effects loosely related to the present discussion include the introduction of residual stresses in gemstone grinding [77], the degradation of brittle surfaces by impact [78] and by laser-induced stress waves [79], and the enhancement of crack growth in semiconductors by photo-activation processes [80].

5.2. Glass cutting

When a glass cutter runs a wheel (tungsten carbide truncated bi-cone) or scribe (diamond point) across a glass surface he aims to produce a well-defined linear "score", after the manner of Fig. 15b, as a starting crack for subsequent plate fracture in bending. This idealized median vent configuration is rarely achieved in practice, however, because of the inevitable presence of inelastic deformation beneath the moving indenter. The residual stresses associated with the deformation zone give rise to lateral vent formation as the indenter unloads (cf. Fig. 12), this being observed experimentally as a splintering (often delayed) about the central cut in the wake of the indenter. (An example of the type of damage produced is shown later, in Fig. 40a.) Lateral vent cracking causes chipping at the edges of the final cut. Quite apart from the issue of aesthetic appearance, a badly chipped edge can act very effectively as a source of stress concentration, with the attendant possibility of premature failure of the cut plate. Attempts in the glass industry to minimize such chipping damage have been based largely on empirical ideas, such as the use of different liquids to "lubricate" the contact system. A more profitable approach might be to look into the possibility of designing the cutting tool in such a way as to enhance median vent growth at the expense of inelastic zone expansion (e.g. by optimizing the ratio of tension to shear or hydrostatic compression below the tool).

5.3. Surface removal processes in brittle materials

In many material shaping and wear processes, particularly where ceramic components are involved, surface matter is removed via a mechanism of localized brittle microfracture. Macroscopic properties such as (the *rate of*, or *resistance to*) abrasion, grinding, drilling, erosion, etc. may therefore be viewed in terms of a summation over a vast number of discrete indentation fracture "tests". Whereas in reality the individual microscopic events will certainly show considerable statistical variation in their degree of effectiveness (and perhaps even in their nature) as a chipping process, and will tend to interact with their neighbours (crack intersection), the indentation test nonetheless serves to provide a physical basis for the general science of material removal processes [81].

The rate at which any such removal process operates depends on many variables, among them the nature of both specimen and indenting particles, the manner of load application, and the environment. Extensive studies of these variables have been made by Westwood and collaborators [82, 83], and by workers in this laboratory [41, 42]. Before attempting a theoretical interpretation of some of the findings in terms of the fundamental concepts of the earlier sections of this paper, we look briefly at some of

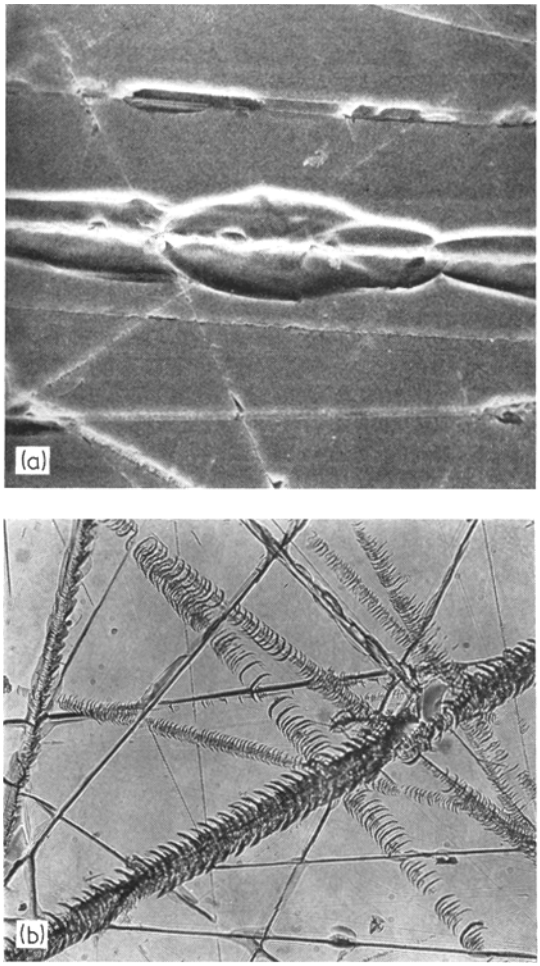

Figure 40 Surface damage on initially polished fused silica, produced under fixed-abrasion conditions. Abrasion medium no. 230 SiC grit paper in *n*-pentanol lubricant. Surfaces etched prior to microscopic examination. (a) Fresh paper, particles sharp (scanning electron microscope), (b) worn paper, particles blunted (reflected light). Width of field 0.25 mm. (Courtesy of G. M. Crimes.)

the variants in the damage patterns observed in different test situations.

5.3.1. Microscopic observations

While there would appear to be no limit to the possible types of surface removal process, we may broadly distinguish between two main categories:

(i) "*Fixed*" *indenting particles.* Where the contacting particles are bonded to some work-tool the resultant surface damage in the specimen tends to resemble that caused by a sliding indenter. This is illustrated in Fig. 40, showing abrasion damage in silica glass produced by bonded silicon carbide paper [41]. In (a), where the abrasive paper used was fresh, several tracks are evident, some of which are very fine and others which show gross chipping. This type of damage is typical of sharp indenters, with chipping occurring when lateral vent cracks intersect the surface. The situation is similar to that described in the preceding section on glass cutting, except that in the present case one actually aims to *promote* rather than to *suppress* the lateral vent system. In (b), where the paper used was well worn, we observe an increasing incidence of broad "chatter sleeks". These are characteristic of the tracks produced by spherical indenters (cf. Fig. 20), indicating a blunting of the abrasive particles. In this case material removal may become significant only when neighbouring cracks link up to form a crazed network.

(ii) "*Free*" *indenting particles.* Where the indenting particles are free to contact the specimen surface without the constraint of rigid bonding to the work-tool, the damage patterns are those which arise from point-localized indentations. Fig. 41 shows further results obtained with silicon carbide on fused silica, this time with the particles in a slurry between work-tool and specimen [41]. In (a), with fresh particles, the scallop-shaped cracks correspond to sharp-indenter damage (cf. Fig. 16), whereas in (b), with worn particles, the cracks resemble the cone fractures typical of blunt indenters (cf. Fig. 19). Crack overlap would again appear to be necessary before significant removal rates could be achieved with blunter, coarser particles.

5.3.2. Role of specific variables

In the light of our present knowledge of indentation fracture processes we might anticipate certain variables to play a vital role in the processes of surface removal. Fig. 42 demonstrates the influence of one of the more obvious of these variables, the applied loading (transmitted by the work-tool to the specimen via the particles), for three brittle solids [84]. The form of the indenter contact (e.g. sharp or blunt, near-normal or sliding, impact or quasi-static) has already been noted in Figs. 40 and 41 to exert a strong influence on the actual removal mechanisms. The mechanical properties of the specimen itself, its degree of brittleness, its

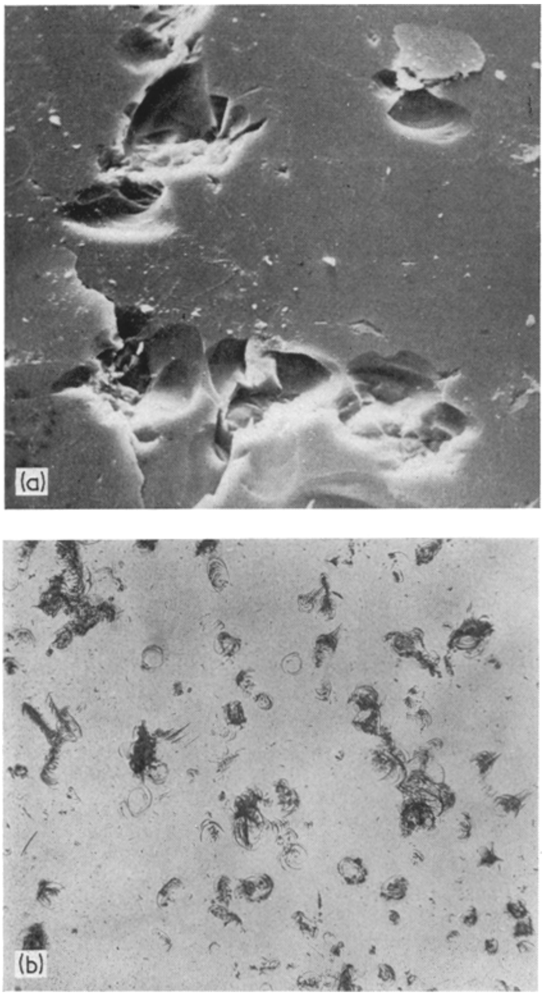

Figure 41 Surface damage on initially polished fused silica, produced under free-abrasion conditions. Abrasion medium no. 230 SiC grit in water slurry. Surface etched prior to microscopic examination. (a) Fresh, sharp particles (scanning electron microscope, width of field 0.25 mm), (b) worn, blunt particles (reflected light, width of field 1.5 mm). (Courtesy G. M. Crimes.)

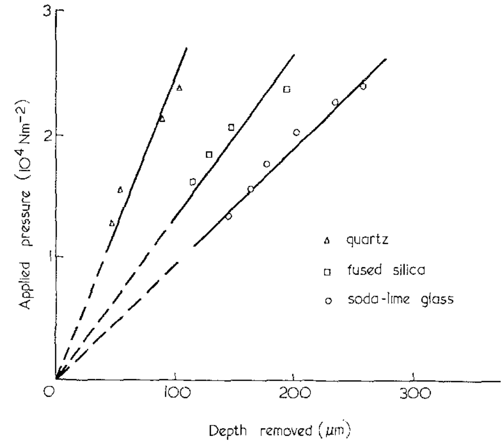

Figure 42 Effect of applied pressure on depth of material removed for different brittle solids under free-abrasion conditions. Abrasion medium no. 550 SiC grit in water slurry. Lapping time 30 min. (After [84].)

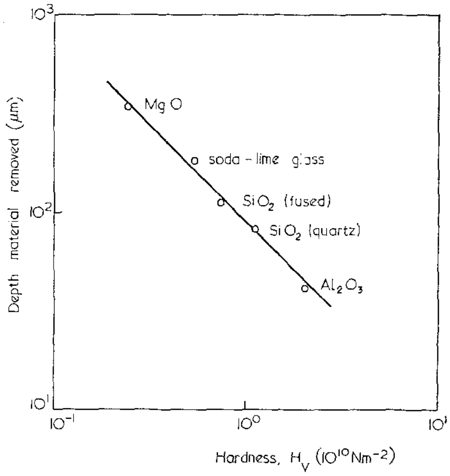

Figure 43 Variation of material removal rate (material removed in standard lapping time) with "static" hardness for a range of brittle solids under free abrasion conditions. Abrasion medium no. 230 SiC grit (freely replenished) in *n*-propanol slurry. Applied pressure 3×10^4 N m^{-2}. (Courtesy G. M. Crimes.)

microstructure (e.g. whether amorphous, mono- or poly-crystalline) etc., will also decide to a greater or lesser extent the geometry and magnitude of the microcracking. Then the working medium (liquid lubricant or slurry) may affect the cracking either directly, via environmental interactions of the type described in Section 4.3, or indirectly, through its frictional and viscous control of the mechanics of particle/specimen contact. Despite the wealth of accumulated data on these variables, interpretations based on sound indentation models remain in their infancy [85, 86].

Of all the variables which enter the general problem, one of the most intriguing is that of material *hardness* [87]. This is seen in the abrasion data of Fig. 43. Assuming the primary removal mechanism to be one of deformation-induced chipping by lateral vent formation beneath a sharp indenter, one may reasonably hypothesize that the volume V_i of the *i*th chip

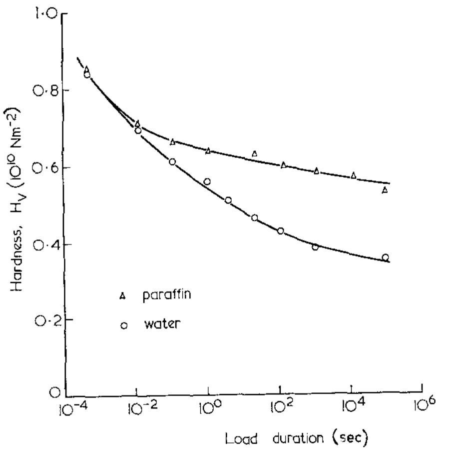

Figure 44 Vickers hardness of cleaved surfaces of float glass as function of load duration in two liquid environments. (After [89].)

must scale with the volume of the inelastic deformation zone (Fig. 12). Then in conjunction with Equation 1, taking $p_0 \approx H$ and the indenter loading and geometry to remain invariant, we may write

$$\left.\begin{array}{ll} V_i \propto a_i^{m3} \propto H^{-3/2}, & \text{(point indentation)} \\ V_i \propto a_i^{m2} \propto H^{-1}, & \text{(linear indentation)} \end{array}\right\} \quad (34)$$

where the superscript m denotes values at maximum loading [9]. Since the removal rate is determined by the sum over all such i events, and H is independent of i, we might expect the dependence in Equation 34 to be reflected in Fig. 43. Actually, the slope in the figure is closer to -1 than to $-3/2$, despite the fact that the data were taken under the free-, point-abrasion conditions represented in Fig. 41a. But in view of the crudity of the model too much weight should not be placed on numerical details.

The reason for the preoccupation with hardness as a variable here is that wide scope exists for control through extraneous influences, with significant improvements in removal rate the ultimate goal. This is the particular aspect of the problem addressed by the Westwood school, in which it is proposed that "near-surface flow" (hence hardness) can be dramatically altered by a suitable choice of environment [82]. That environmental effects have an important bearing on hardness values is indisputable, as shown on a variety of solids by Hanneman and Westbrook [88] and in special detail on glass by Gunasekera and Holloway [89]; data from the latter source are presented in Fig. 44 for a very wide range of indentation times. The effect here is clearly a kinetic one, and it becomes necessary to take into account the time element in any detailed mechanical analysis of the removal mechanism. For instance, in a typical free-abrasion operation the average duration of contact between indenting particle and specimen surface is 10^{-3} to 10^{-4} sec [90] (that is, approaching a dynamical contact regime, cf. Fig. 8); environmental effects have little time to manifest themselves in this regime, as evidenced by the merging of the two curves at the left of Fig. 44. Therefore, it is apparent that the near-surface flow concept, indeed any kinetic chemomechanical concept, should not be applied without due consideration of the contact mechanics appropriate to a given system.

5.4. Efficiency of particle size reduction by fragmentation (comminution)

The production of particulate matter involves the creation of new surfaces by a variety of contrived contact loading systems: ore crushing, rock drilling, ball or rod milling, etc., are examples, processes which may operate on a massive scale of industrial manufacture. The questions of performance and efficiency assume a central position in the evaluation of any such large-scale process.

Basically, the efficiency of a given fragmentation or comminution system may be assessed as the proportion of the work done on the system which goes into creating new particle surface [90]. Using the fracture-mechanics terminology of Section 3 we may conveniently define the efficiency as $\epsilon = U_S/W_L$, U_S being the total surface energy of the new particles and W_L the total work done by applied forces. Typically, industrial comminution processes operate at an efficiency of only a few percent (with most of the energy input dissipated as heat). There would, therefore, appear to be wide scope for greater efficiencies, such that even minor improvements in technological technique could lead to substantial savings in production costs.

In view of the great complexity of most comminution processes it is hardly surprising that quantitative models have been slow in evolving. However, the indentation fracture treatment given in the earlier sections of this paper does suggest a particularly simple working model (Fig. 45). From the experimental standpoint one tries to simulate practical behaviour in tests where single particles are loaded to failure

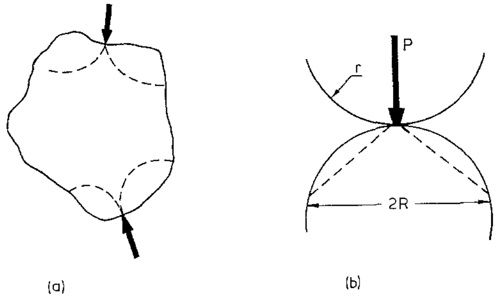

Figure 45 Schematic model of brittle chipping by attrition: (a) irregular particle under localized crushing forces, (b) idealized cone-crack representation.

in compression [91, 92]. The results of such tests indicate that much of the fragmentation occurs by attrition, as depicted in Fig. 45a, and this is borne out by the examination of particles removed from production systems (where the crushing agent may be another particle, or some suitable percussive body such as ball, rod, or roller). Theoretically, one represents the practical situation by the idealization of Fig. 45b (cf. Fig. 24). This opens the way to an analysis in terms of cone-crack parameters. The elastic work done on the contact system by the applied force P is

$$W_L = \int_0^Z P(Z)\mathrm{d}Z\,, \qquad (35)$$

where Z is the mutual approach distance given by Equation 6*. Integration of Equation 35 then gives

$$W_L = \frac{2}{5}\left(\frac{4k}{3E}\right)^{2/3}\left(\frac{P^5}{r}\right)^{1/3}\cdot \qquad (36)$$

The function $P(Z)$ is found in practice to be remarkably insensitive to the sudden appearance of the cone crack, so Equation 36 may be taken as perfectly general for the entire elastic/brittle contact. For well-developed cones the total surface energy of the crack faces is

$$U_S = \left(\frac{2\pi R^2}{\cos\alpha}\right)\Gamma\cdot \qquad (37)$$

Observation of glass spheres in compression [91] shows that the approach to failure is by stable growth of the cone, essentially according to the Roesler configuration of Section 3.2.2, to $R \approx r$ (Fig. 45b). Thus, dividing Equation 36 into Equation 37, and eliminating P through Equation 25, we obtain as an approximate estimate of the efficiency,

$$\epsilon = \frac{U_S}{W_L} = \frac{5\pi}{4\cos\alpha}\left(\frac{81\kappa^5\Gamma}{2k^4rE}\right)^{1/6}\cdot \qquad (38)$$

To illustrate the quantitative significance of Equation 38 we consider a system involving glass particles, $r = 100\ \mu\text{m}$, $E = 7 \times 10^{10}\ \text{N m}^{-2}$ and $\Gamma = 4\ \text{J m}^{-2}$ (values used in Section 3.2), $k = 1$ (like particles, Equation 5), $\kappa = 1.3 \times 10^{-3}$ (calibrated value, Section 3.2.2), $\alpha = 22°$, to obtain $\epsilon \approx 0.03$. This is of the order of the efficiency of the typical comminution process, as mentioned earlier. However, apart from serving as a convenient means for evaluating an absolute figure of merit, this type of calculation points the way as to how the efficiency might actually be increased. Accordingly, by incorporating relatively rigid percussive bodies into the system and thereby diminishing the parameter k (minimum value 0.5, for *perfectly* rigid indenter, Equation 5), small but significant increases in ϵ may obtain. Systematic consideration of such models is a promising topic for the future.

Acknowledgements

We are indebted to many students and colleagues for their co-operation in the preparation of this review. B. R. Lawn acknowledges receipt of a Science Research Council (U.K.) Fellowship.

References

1. D. TABOR, *Rev. Phys. Tech.* **1** (1970) 145.
2. J. H. WESTBROOK and H. CONRAD, Eds., "The Science of Hardness Testing and its Research Applications", Symposium Proceedings (American Society for Metals, Metals Park, Ohio, 1973).
3. H. HERTZ, *J. Reine Angew. Math.* **92** (1881) 156; *Verhandlungen des Vereins zur Beförderung des Gewerbe Fleisses* **61** (1882) 449. Reprinted, in English, in "Hertz's Miscellaneous Papers" (Macmillan, London, 1896) Chs. 5, 6.
4. A. A. GRIFFITH, *Phil. Trans. Roy. Soc. Lond.* **A221** (1920) 163.
5. D. TABOR, "The Hardness of Metals" (Clarendon, Oxford, 1951).
6. I. N. SNEDDON, "Fourier Transforms" (McGraw-Hill, New York, 1951).
7. K. L. JOHNSON, *J. Mech. Phys. Solids* **18** (1970) 115.
8. J. BOUSSINESQ, "Application des Potentiels a l'Etude de l'Equilibre et du Mouvement des Solides Elastiques" (Gauthier-Villars, Paris, 1885). Discussed in S. P. TIMOSHENKO and J. N. GOODIER, "Theory of Elasticity" (McGraw-Hill, New York, 1970) pp. 398-402.

---

*Strictly, for two spherical bodies in contact, the radius r in Equation 6 should be replaced by the harmonic mean $r_1r_2/(r_1+r_2)$[3].

9. B. R. LAWN and M. V. SWAIN, *J. Mater. Sci.*, **10** (1975) 113.
10. B. R. LAWN and T. R. WILSHAW, "Fracture of Brittle Solids" (Cambridge University Press, Cambridge, 1975).
11. B. R. LAWN, T. R. WILSHAW and N. E. W. HARTLEY, *Int. J. Fract.* **10** (1974) 1.
12. M. T. HUBER, *Ann. Physik* **14** (1904) 153.
13. F. C. FRANK and B. R. LAWN, *Proc. Roy. Soc. Lond.* **A299** (1967) 291.
14. B. R. LAWN, *J. Appl. Phys.* **39** (1968) 4828.
15. J. J. H. BEEK and B. R. LAWN, *J. Phys. E: Sci. Instrum.* **5** (1972) 710.
16. C. M. LEVITT and F. R. N. NABARRO, *Proc. Roy. Soc. Lond.* **A293** (1966) 259.
17. K. L. JOHNSON, J. J. O'CONNOR and A. C. WOODWARD, *ibid* **A334** (1973) 95.
18. J. A. GREENWOOD and J. H. TRIPP, *J. Appl. Mech.* **89** (1967) 153.
19. G. M. HAMILTON and L. E. GOODMAN, *ibid* **33** (1966) 371.
20. B. R. LAWN, *Proc. Roy. Soc. Lond.* **A299** (1967) 307.
21. D. M. MARSH, *ibid* **A279** (1964) 420.
22. J. H. WESTBROOK, *J. Amer. Ceram. Soc.* **41** (1958) 433.
23. E. A. ALMOND and B. ROEBUCK, "Scanning Electron Microscopy: Systems and Applications", Conference Proceedings (Institute of Physics, London, 1973) p. 106.
24. A. G. MIKOSZA and B. R. LAWN, *J. Appl. Phys.* **42** (1971) 5540.
25. T. R. WILSHAW, *J. Phys. D: Appl. Phys.* **4** (1971) 1567.
26. F. C. ROESLER, *Proc. Phys. Soc.* **B69** (1956) 981.
27. C. J. CULF, *J. Soc. Glass Tech.* **41** (1957) 157.
28. J. J. BENBOW, *Proc. Phys. Soc.* **B75** (1960) 697.
29. J. S. WILLIAMS, B. R. LAWN and M. V. SWAIN, *Phys. Stat. Sol.* (*a*) **2** (1970) 7.
30. A. V. SHUBNIKOV and K. ZINSERLING, *Z. Krist.* **83** (1932) 243.
31. N. E. W. HARTLEY and T. R. WILSHAW, *J. Mater. Sci.* **8** (1973) 265.
32. J. W. HEAVENS, Ph.D. Thesis, University of Bristol (1972).
33. K. H. G. ASHBEE, unpublished work.
34. V. R. HOWES and S. TOLANSKY, *Proc. Roy. Soc. Lond.* **A230** (1955) 287, 294.
35. S. TOLANSKY and V. R. HOWES, *Proc. Phys. Soc.* **B70** (1957) 521.
36. V. R. HOWES, "Physical Properties of Diamond", edited by R. Berman (Clarendon, Oxford, 1965) Ch. 6.
37. B. R. LAWN and H. KOMATSU, *Phil. Mag.* **14** (1966) 689.
38. O. W. JOHNSON, *J. Appl. Phys.* **37** (1966) 2521.
39. E. N. PUGH and L. E. SAMUELS, *Phil. Mag.* **8** (1963) 301.
40. J. W. ALLEN, *ibid* **4** (1959) 1046.
41. G. M. CRIMES, Ph.D. Thesis, University of Sussex (1973).
42. K. PHILLIPS, Ph.D. Thesis, University of Sussex (1975).
43. M. V. SWAIN and B. R. LAWN, *Phys. Stat. Sol.* **35** (1969) 909.
44. C. J. STUDMAN, Ph.D. Thesis, Cambridge University (1974).
45. K. E. PUTTICK, L. E. MILLER and E. GILLHAM, to be published.
46. B. R. LAWN, *J. Mater. Sci.* **10** (1975) 469.
47. S. M. WIEDERHORN, *J. Amer. Ceram. Soc.* **52** (1969) 99.
48. M. V. SWAIN and B. R. LAWN, *Int. J. Fract.* **9** (1973) 481.
49. B. R. LAWN, in [2] Ch. 29.
50. F. AUERBACH, *Ann. Phys. Chem.* **43** (1891) 61.
51. F. C. ROESLER, *Proc. Phys. Soc.* **B69** (1956) 55.
52. J. P. A. TILLET, *ibid* **B69** (1956) 47.
53. F. B. LANGITAN and B. R. LAWN, *J. Appl. Phys.* **40** (1969) 4009.
54. M. SEAL, *Proc. Roy. Soc. Lond.* **A248** (1958) 379.
55. J. S. NADEAU, *J. Amer. Ceram. Soc.* **56** (1973) 467.
56. B. D. POWELL and D. TABOR, *J. Phys. D: Appl. Phys.* **3** (1970) 783.
57. F. B. LANGITAN and B. R. LAWN, *J. Appl. Phys.* **41** (1970) 3357.
58. T. R. WILSHAW and R. ROTHWELL, *Nature, Lond.* **229** (1971) 156.
59. S. PALMQVIST, *Jernkontorets Ann.* **141** (1957) 300.
60. *Idem, Arch. Eisenhuttenw.* **33** (1962) 629.
61. H. E. EXNER, *Trans. Met. Soc. AIME* **245** (1969) 677.
62. M. V. SWAIN, J. S. WILLIAMS, B. R. LAWN and J. J. H. BEEK, *J. Mater. Sci.* **8** (1973) 1153.
63. J. S. NADEAU and A. S. RAO, *J. Canad. Ceram. Soc.* **41** (1972) 63.
64. B. R. LAWN, T. R. WILSHAW, T. I. BARRY and R. MORRELL, *J. Mater. Sci.* **10** (1975) 179.
65. J. S. WILLIAMS and B. R. LAWN, *ibid* **8** (1973) 1059.
66. S. M. WIEDERHORN and L. H. BOLZ, *J. Amer. Ceram. Soc.* **53** (1970) 543.
67. N. GANE and F. P. BOWDEN, *J. Appl. Phys.* **39** (1968) 1432.
68. K. W. PETER and E. DICK, *Glastechn. Ber.* **40** (1967) 470.
69. A. S. ARGON, *Proc. Roy. Soc. Lond.* **A250** (1959) 482.
70. E. W. SUCOV, *J. Amer. Ceram. Soc.* **45** (1962) 214.
71. J. D. POLONIECKI and T. R. WILSHAW, *Nature, Lond.* **229** (1971) 226.
72. Y. M. TSAI and H. KOLSKY, *J. Mech. Phys. Solids* **15** (1967) 29.
73. H. L. OH and I. FINNIE, *ibid* **15** (1967) 401.
74. B. HAMILTON and H. RAWSON, *ibid* **18** (1970) 127.
75. S. J. BLOOMER, Final-year Report, University of Sussex (1974).
76. W. E. SWINDLEHURST, Ph.D. Thesis, University of Sussex (1974).
77. F. C. FRANK, B. R. LAWN, A. R. LANG and E. M. WILKS, *Proc. Roy. Soc. Lond.* **A301** (1967) 239.
78. A. G. EVANS, *J. Amer. Ceram. Soc.* **56** (1973) 405.

79. P. B. WITHERS and T. R. WILSHAW, *J. Phys. D: Appl. Phys.* **6** (1973) 322.
80. C. N. AHLQUIST and L. CARLSSON, *Phil. Mag.* **28** (1973) 733.
81. "The Science of Ceramic Machining and Surface Finishing", Symposium Proceedings (N.B.S. Special Publ. 348, 1972).
82. A. R. C. WESTWOOD and N. H. MACMILLAN, in [2], Ch. 28.
83. A. R. C. WESTWOOD, *J. Mater. Sci.* **9** (1974) 1871.
84. T. R. WILSHAW and N. E. W. HARTLEY, "Third European Symposium on Comminution" (Verlag Chemie, GMBH, Weinheim/Bergstrasse, 1972) Vol. 1, p. 33.
85. H. L. OH, K. P. L. OH, S. VAIDYANATHAN and I. FINNIE, in [81], p. 119.
86. G. L. SHELDON and I. FINNIE, *Trans. ASME* **88B** (1966) 393.
87. T. IZUMITANI and I. SUZUKI, *Glass Technol.* **14** (1973) 35.
88. R. E. HANNEMAN and J. H. WESTBROOK, *Phil. Mag.* **18** (1968) 73.
89. S. P. GUNASEKERA and D. G. HOLLOWAY, *Phys. Chem. Glasses* **14** (1973) 45.
90. T. R. WILSHAW, G. M. CRIMES and K. PHILLIPS, Paper presented at Symposium on the Strength of Glass and Glassware, University of Sussex, March 1974.
91. H. RUMPF, "Third European Symposium on Comminution" (Verlag Chemie, GMBH, Weinheim/Bergstrasse, 1972) Vol. 1, p. 51.
92. H. RUMPF, *Aufbereitungs-Technik* **2** (1973) 3.

Received 1 October and accepted 18 October 1974.